Growth of vortical disturbances entrained in the entrance region of a circular pipe

Pierre Ricco[1]† and Claudia Alvarenga[1,2]

[1]Department of Mechanical Engineering, The University of Sheffield, S1 3JD Sheffield, United Kingdom

[2]Department of Fluid Dynamics, A*Star Institute of High Performance Computing, Singapore

The development and growth of unsteady three-dimensional vortical disturbances entrained in the entry region of a circular pipe is investigated by asymptotic and numerical methods for Reynolds numbers between 1000 and 10000, based on the pipe radius and the bulk velocity. Near the pipe mouth, composite asymptotic solutions describe the dynamics of the oncoming disturbances, revealing how these disturbances are altered by the viscous layer attached to the pipe wall. The perturbation velocity profiles near the pipe mouth are employed as rigorous initial conditions for the boundary-region equations, which describe the flow in the limit of low frequency and large Reynolds number. The disturbance flow is initially primarily present within the base-flow boundary layer in the form of streamwise-elongated vortical structures, i.e., the streamwise velocity component displays an intense algebraic growth, while the cross-flow velocity components decay. Farther downstream the disturbance flow occupies the whole pipe, although the base flow is mostly inviscid in the core. The transient growth and subsequent viscous decay are confined in the entrance region, i.e., where the base flow has not reached the fully developed Poiseuille profile. Increasing the Reynolds number and decreasing the frequency causes more intense perturbations, whereas small azimuthal wavelengths and radial characteristic length scales intensify the viscous dissipation of the disturbance. The azimuthal wavelength that causes the maximum growth is found. The velocity profiles are compared successfully with available experimental data and the theoretical results are helpful to interpret the only direct numerical dataset of a disturbed pipe-entry flow.

Key words:

---

1. Introduction

The problem of the stability and transition to turbulence of pipe flows has witnessed an immense interest in the scientific and engineering communities since the famous experimental work of Reynolds (1883). Flows through pipes are central to countless engineering applications, primarily because one must predict the occurrence of transition to turbulence as the majority of gas, oil, water and air pipe flows are turbulent even at moderate Reynolds numbers. While fluids engineers are mostly concerned with an accurate computation of the pressure gradient required for propelling the fluid through

† Email address for correspondence: p.ricco@sheffield.ac.uk

pipes, physicists and mathematicians have also been attracted by the fascinating physical phenomena observed in these flows and by the exceptional difficulties related to the theoretical analysis of these confined flows.

It is still not clear how a laminar pipe flow becomes unstable and evolves to turbulence. The first theoretical challenge is that numerical and theoretical studies have consistently reported that the Poiseuille laminar flow is always stable to small perturbations at every Reynolds number when the problem is investigated using classical stability theory (Drazin & Reid 2004). This result has therefore led researchers to analyse the dynamics of finite-amplitude disturbances and alternative routes to turbulence.

Research studies on pipe flows have mainly focussed on the dynamics of the fully developed laminar flow, while a limited number of investigations have reported results on the entrance problem, that is, where the laminar base flow evolves from the pipe mouth. Along the entrance region, the flow depends on the streamwise coordinate and the pressure gradient is unknown a priori, thus posing additional challenges to its analysis. Our main objectives are, therefore, to investigate how vortical disturbances superimposed on the oncoming base flow at the pipe entrance are influenced by the pipe confinement, and how they are convected and evolve downstream through the pipe along the entrance region, prior to the flow breakdown to turbulence. We have devoted particular attention to the flow specification at the pipe mouth because a realistic source of perturbation is fundamental as a first step towards a full understanding of the pipe-flow transition to turbulence. We have considered the pipe wall to be smooth, rigid and stationary, and therefore we have neglected two other realistic sources of disturbances, i.e., wall roughness and wall vibrations.

In the following, we first discuss the most relevant studies of stability and transition in pipe flows and then we present our research objectives and the structure of the paper.

1.1. *Stability of fully developed pipe flows: small perturbations*

Motivated by the impact of the pioneering experiments by Reynolds (1883), Rayleigh (1892) conducted the first stability analysis of a cylindrical flow in the inviscid regime, finding only stable perturbations. The first viscous stability study was carried out years later by Sexl (1927), who showed flow stability in the limits of small and large Reynolds numbers. Several studies in the past century, such as Pekeris (1948), Corcos & Sellars (1959), Gill (1965), Lessen *et al.* (1968), Crowder & Dalton (1971) and Salwen *et al.* (1980), have established that the fully developed Poiseuille pipe flow is stable to infinitesimal disturbances according to classical stability theory even at very large Reynolds number. It was therefore a natural step to analyse other mechanisms of instability, such as transiently growing disturbances. Bergström (1993), Schmid & Henningson (1994), O'Sullivan & Breuer (1994), Mayer & Reshotko (1997), Trefethen *et al.* (1999) and Meseguer (2003) studied the transient problem in time, while Reshotko & Tumin (2001) focussed on the spatial transient evolution of the disturbances. The results of Mayer & Reshotko (1997) are of note as they compare favourably with the experimental results by Kaskel (1961). These studies concur that small perturbations superimposed on the fully developed Poiseuille flow can grow algebraically in time or space and then decay because of viscous effects. The reader is referred to section 3.2 in Kerswell (2005) for an exhaustive discussion of stability studies of small perturbations superimposed on the Poiseuille flow.

Alongside the theoretical advancements, pipe-flow experimental campaigns followed the work of Reynolds (1883), as summarized in section 3.1 of Kerswell (2005). Fox *et al.* (1968) experimentally tested the stability of small perturbations introduced in the fully developed region and reported that the flow became unstable for Reynolds

numbers larger than approximately 2000 (based on the pipe diameter), i.e., comparable with the results found by Reynolds (1883), although no comparison was carried out because the perturbations of Reynolds (1883)'s experiments were at the pipe inlet. Other experimental campaigns, e.g. Draad *et al.* (1998), demonstrated that the transition Reynolds number could be increased significantly by reducing the amplitude of the perturbations.

1.2. *Stability and transition of fully developed pipe flows: finite-amplitude perturbations*

As linearized dynamics only provided a limited understanding of the fully developed pipe-flow transition problem, considerable effort has been devoted to the nonlinear behaviour of perturbations. The dynamics of finite amplitude disturbances in the limit of high Reynolds number was first studied by Davey & Nguyen (1971) via weakly nonlinear theory. The equilibrium perturbation amplitude above which disturbances grow was predicted and the most unstable disturbance was found to be near the pipe axis. These results were contradicted by Itoh (1977), who discovered no equilibrium states by a similar approach. Davey (1978) further analysed these studies and concluded that neither centre-mode results were reliable, although maintained that equilibrium states did exist. Smith & Bodonyi (1982) indeed found neutral disturbances of finite amplitude by utilizing nonlinear critical layer theory. Patera & Orszag (1981), using direct numerical simulations, did not find any axisymmetric equilibrium states and concluded that the weakly nonlinear approach can lead to invalid results.

Nonlinear travelling waves were first discovered numerically by Faisst & Eckhardt (2003) and Wedin & Kerswell (2004), thus paving the way for the use of dynamical systems in the study of pipe-flow transition (Duguet *et al.* 2008; Hof *et al.* 2008; Avila *et al.* 2010, 2013). Section 4 in Kerswell (2005) discusses the main results on these travelling waves. Their existence was confirmed in the water pipe-flow experiments of Hof *et al.* (2004, 2005).

Other useful papers that thoroughly discuss experimental, numerical and theoretical advances related to the pipe-flow problem in the nonlinear regime are those by Avila *et al.* (2011), Eckhardt *et al.* (2007), Eckhardt (2009), Avila *et al.* (2011) and Mullin (2011). The review paper by Eckhardt (2007) offers an interesting list of open problems related to the pipe-flow nonlinear breakdown to turbulence.

1.3. *Stability and transition of pipe-entrance flows*

As Reynolds (1883) recognized that the perturbance dynamics from the pipe inlet played a key role in the flow breakdown to turbulence, researchers have turned their attention to the stability of the pipe entrance flow. The main conclusion is that the pipe entrance flow is linearly unstable according to classical stability theory (Tatsumi 1952; Huang & Chen 1974*b,a*; Smith & Bodonyi 1980; Garg 1981; Gupta & Garg 1981; da Silva & Moss 1994), although there is still controversy about the exact form of the neutral curve, inside which Tollmien-Schlichting (TS) waves appear. The results by Gupta & Garg (1981) and da Silva & Moss (1994) show good agreement for most of the downstream locations and Reynolds numbers, from which it has been concluded that the entrance flow is linearly stable for Reynolds numbers smaller than approximately 10000, based on the pipe radius and bulk velocity. Much lower critical Reynolds numbers have been reported by the experimental study of Sarpkaya (1975), probably because of the finite size of the induced perturbation, and by the numerical investigation of Sahu & Govindarajan (2007). Duck (2005, 2006) used asymptotic and numerical methods to study the algebraic growth of disturbances near the pipe mouth, in the form of the so-called Luchini mode (Luchini 1996), located within the boundary layer attached to the pipe wall.

Wygnanski & Champagne (1973)'s experimental study focussed on the initial growth of perturbations generated at the pipe mouth, with the objective of understanding how these disturbances seeded turbulent puffs and slugs farther downstream. More laboratory data have been reported by Zanoun *et al.* (2009) in an attempt to quantitatively correlate the location and features of the transitional flow with the intensity of the inlet perturbations. The direct numerical simulations by Wu *et al.* (2015) and Wu *et al.* (2020) showed how localized perturbations imposed at the pipe entrance evolved downstream and led to the breakdown to turbulence. At the pipe inlet, the Poiseuille parabolic velocity profile was chosen as base profile in most of the cases, and the uniform plug flow was selected in one case.

To the best of the authors' knowledge, no theoretical studies exist on the entrainment of velocity and pressure perturbations at the pipe inlet, in an attempt to analyse how these disturbances evolve and grow downstream inside the confined space.

1.4. *Objectives and structure of the paper*

We aim to analyse the response of the entrance incompressible pipe flow to vortical disturbances convected by the inlet flow. The main motivation arose from the absence of theoretical results on the dynamics of pipe entrance flows perturbed by disturbances that can be created and measured in a laboratory, despite the central role played by these perturbations as harbingers of instability and transition, as recognized since the pioneering work of Reynolds (1883). We consider flows at Reynolds numbers for which the entrance pipe flow is stable according to classical stability theory, i.e., TS waves do not occur, although experimental results have shown these flows to transition to turbulence.

We adopt the reasonable assumptions of large Reynolds number and of velocity disturbances of small amplitude and low frequency. The last assumption is based on the observation that streamwise-stretched low-frequency perturbations are the most likely to penetrate viscous layers and amplify downstream to cause transition (Matsubara & Alfredsson 2001). We are particularly interested in explaining how the disturbances are altered as they enter the pipe confinement and experience the increasing base-flow pressure gradient, how they penetrate into the boundary layer attached to the pipe wall, and how they amplify inside the pipe as the base flow becomes fully developed. We report how the perturbation dynamics depends on the flow parameters, such as the Reynolds number, the frequency, and the wavelengths of the prescribed disturbance. We carry out visual and data-based comparisons with experimental data of Wygnanski & Champagne (1973), and interpret results from the direct numerical simulation study of Wu *et al.* (2015) on a pipe flow perturbed by inlet disturbances.

Our mathematical approach and numerical results are a starting point for the understanding of the relationship between the transitional Reynolds number and the role of inlet vortical perturbations in laminar-to-turbulent transition in pipe flows. We have restricted the analysis to the linearized dynamics under the assumption of small perturbations and we are currently extending our study to the nonlinear case.

In §2, the scaling and assumptions are presented, together with the governing equations and the numerical procedures. The initial flow development is studied in §3 and the results of the downstream flow dynamics are discussed in §4. The conclusions of our study are presented in §5.

2. Scaling and equations of motion

We first present the asymptotic scaling in §2.1 and the equations of motion in §2.2. In §2.3 we discuss how linear stability results are useful to extract the locations in the

entrance pipe-flow region where exponentially growing waves may occur. The numerical procedures are discussed in the Supplementary Material S1.

2.1. *Scaling and asymptotic regions*

We consider the pressure-driven incompressible flow at the entrance of a pipe with circular cross-section. Dimensional quantities are hereafter indicated by the superscript $*$. The oncoming flow approaching the pipe entrance is assumed to be uniform, of velocity U_∞^* and aligned with the pipe axis. The pipe wall is assumed to be infinitely thin so that, similar to the case of uniform flow approaching a thin flat wall, the oncoming flow is undisturbed at leading order. In a laboratory, the upstream geometry and the finite thickness of the pipe wall may alter the uniformity of the oncoming flow. Our inlet flow, therefore, is a simplified version of that utilized by O. Reynolds in his seminal study (Reynolds 1883), where the pipe entrance was bell shaped. As the oncoming flow enters the pipe, a boundary layer develops on the pipe wall. The thickness of this viscous layer increases downstream until the pipe flow becomes fully viscous and attains the classical Poiseuille parabolic profile.

The flow is conveniently represented in a cylindrical coordinate system, where the coordinates x^*, r^* and θ are the streamwise direction, the radial direction and the azimuthal angle, respectively. The centreline of the pipe is at $r^* = 0$ and the pipe wall is located at $r^* = R^*$, where R^* is the pipe radius. Lengths are scaled by a reference length λ^*, specified below. Velocities are normalized by U_∞^*, the pressure is scaled by $\rho^* U_\infty^{*2}$, where ρ^* is the density of the fluid, and the time is scaled by λ^*/U_∞^* (quantities without any symbols are non-dimensional).

Superimposed on the oncoming streamwise flow $\{U_\infty^*, 0, 0\}$ are gust-type vortical fluctuations advected by the base flow. In a technological or industrial system, these oncoming disturbances could be due to upstream vibrations or structural imperfections, and in a laboratory setting they could be generated by vibrating ribbons or rigid grids located near the pipe entrance, where the wavelengths and frequencies could be controlled accurately, as could the location of generation.

We first consider a region around the pipe axis where velocity fluctuations are not influenced by the pipe wall, either by the no-penetration condition on the radial velocity disturbance or by the no-slip condition on the streamwise and azimuthal velocity components. At these locations sufficiently near $x = 0$ and sufficiently far away from the pipe wall, the velocity fluctuations can be expressed mathematically as a Fourier–Bessel series, where the Fourier expansions pertain to time, x and θ, while the Bessel expansion is used along the radial coordinate. As it is assumed that the amplitude of the perturbation is asymptotically smaller than U_∞^*, the perturbation dynamics is linear. A single Fourier–Bessel coefficient of the full-spectrum series expansion is thus considered, as follows

$$\mathbf{u} = \{1, 0, 0\} + \varepsilon \left\{ \hat{u}_{x,mn}^\infty J_m\left(\overline{r}\right), \frac{\hat{u}_{r,mn}^\infty J_m\left(\overline{r}\right)}{\overline{r}}, \frac{-i\hat{u}_{\theta,mn}^\infty J_m'\left(\overline{r}\right)}{\xi_{mn}} \right\} e^{i[k_x(x-t)+m\theta]} + \text{c.c.}, \quad (2.1)$$

where J_m is the Bessel function of the first kind of order m, $E = e^{i[k_x(x-t)+m\theta]}$, $\varepsilon \ll 1$ is the amplitude of the gust, $\overline{r} = \xi_{mn} r/2R$, ξ_{mn} are the zeros of the Bessel function, i.e. the real numbers that satisfy $J_m(\xi_{mn}) = 0$, c.c. stands for the complex conjugate, and the prime indicates the first derivative with respect to $\overline{r}$. In the most general case, the quantities $\left\{ \hat{u}_{x,jmn}^\infty, \hat{u}_{r,jmn}^\infty, \hat{u}_{\theta,jmn}^\infty \right\} = \mathcal{O}(1)$ are complex. The inviscid velocity field (2.1) satisfies the Euler equations and is generated at a circle of radius $2R$, centred at the pipe centreline and located in the plane (r, θ) at a small distance upstream of the pipe

mouth at $x = 0$. The scaling of the radial direction by $2R$ is used instead of R to avoid the unrealistic scenario of vanishing streamwise and radial velocity components at $r = R$ where the disturbance is generated.

The reference length is $\lambda^* = \theta_g R^*$ ($\lambda^*/R^* = \mathcal{O}(1)$), that is, the circumferential wavelength of the gust at $r^* = R^*$, where θ_g is the azimuthal angle corresponding to the wavelength λ^*. As in the flat-plate case of Leib *et al.* (1999) where the spanwise wavelength is used, the azimuthal wavelength λ^* at $r^* = R^*$ is chosen because downstream it becomes comparable with the boundary layer thickness and the pipe radius. If $\theta_g = \pi/2$, the wavelength λ^* spans a quarter of the circumference of the pipe. An obvious constraint is that the maximum λ^* coincides with the pipe circumference. The coefficient $m = 2\pi R \in \mathbb{N}$ denotes the number of wavelengths λ^* around the circumference (we restrict ourselves to cases for which $m \neq 0$ because we are interested in three-dimensional disturbances). The radial velocity is never singular at the centreline despite J_m being divided by $\bar{r}$ because, given $J_m(\bar{r}) \sim (\bar{r}/2)^m/\Gamma(m+1)$ for $\bar{r} \ll 1$ (where Γ is the gamma function), the radial average $\hat{u}_{r,0n}^{\infty}$ is zero.

The focus is on low-frequency (i.e. long wavelength) disturbances with a streamwise wavenumber $k_x = 2\pi\lambda^*/\lambda_x^* \ll 1$, where λ_x^* is the streamwise wavelength of the gust, as these perturbations are most likely to penetrate a boundary layer and generate laminar streaks (Matsubara & Alfredsson 2001). As the convected gust is transported passively by the uniform base flow, the pressure fluctuations are negligible at leading order in $k_x \ll 1$ (refer to Goldstein (1978), equation (2.3) and Leib *et al.* (1999), equation (3.2)). Equation (2.1) satisfies the continuity equation as the term emerging from $\partial u/\partial x$ is $\mathcal{O}(k_x) \ll 1$, i.e.

$$\xi_{mn}\hat{u}_{r,mn}^{\infty} + m\hat{u}_{\theta,mn}^{\infty} = \mathcal{O}(k_x). \tag{2.2}$$

Without losing generality, $m > 0$ is taken. The continuity equation also determines the $\bar{r}^{-1}$ dependence for the radial velocity and the dependence on the derivative of the Bessel function and the coefficient $-i/\xi_{mn}$ for the the azimuthal velocity.

The Reynolds number is $Re_\lambda = U_\infty^*\lambda^*/\nu^* \gg 1$. Inside the pipe, the disturbances evolve downstream on a length scale that is comparable with the streamwise gust wavelength. A distinguished scaling is thus $k_x = \mathcal{O}(Re_\lambda^{-1})$ or $\bar{x} = k_x x = 2\pi x^*/\lambda_x^* = \mathcal{O}(1)$. The disparity between the streamwise and azimuthal scales implies that disturbances of amplitude $\mathcal{O}(\varepsilon)$ may generate streamwise velocity perturbations with an amplitude of $\mathcal{O}(\varepsilon/k_x)$ in the viscous layers. These amplitudes are assumed to be much smaller than U_∞^*, which translates to $\varepsilon/k_x \ll 1$ or $\varepsilon Re_\lambda \ll 1$ and implies that the Navier-Stokes equations may be linearized.

Vortical disturbances analogous to those defined in (2.1) have been found in other cylindrical flows, i.e. the instability modes of a rotating pipe flow also have the streamwise velocity component proportional to J_m and the radial velocity proportional to J_m/r (Pedley 1969). A similar choice for the oncoming disturbance was employed for the flat-plate boundary-layer cases studied by Ricco *et al.* (2011) and Marensi *et al.* (2017), who prescribed the vorticity fluctuations as a pair of gusts with equal and opposite spanwise wavenumbers. Disturbances (2.1) are physically realistic because they may be generated, for example, by a grid at the entry of the pipe, as a circular analogue to the vibrating wires used in the receptivity studies by Dietz (1999) and Borodulin *et al.* (2021*a,b*) for two- and three-dimensional free stream vortical disturbances, respectively.

As shown in figure 1, the domain is divided into six asymptotic regions. The effect of the base-flow streamwise pressure gradient is negligible in regions I, II and III, mild in region IV, and fully influential in region V. In region VI, the base flow is fully developed. In region I, at $x = \mathcal{O}(1)$, the base and the perturbation flows are inviscid and rapid distortion
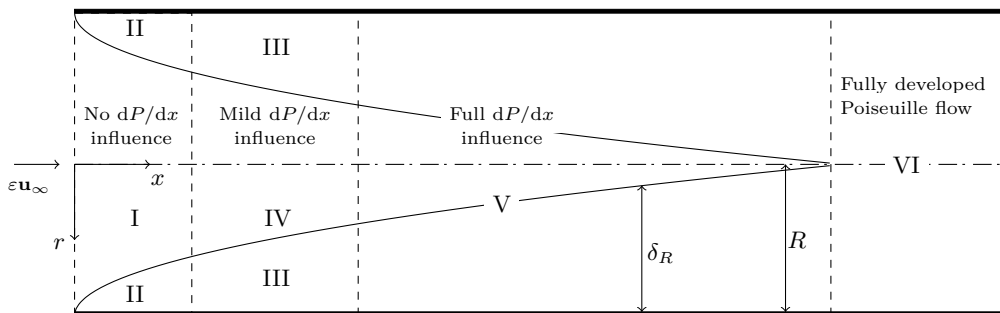
Figure 1: Asymptotic regions of the pipe flow (not in scale). The boundary-layer thickness δ_R is defined in §4.1.

theory applies (Goldstein 1978). A velocity potential is used and the wall is taken into account through the no-penetration condition on the radial velocity component. In the viscous region II, $\delta^*/\lambda^* \ll 1$, where δ^* is the boundary-layer thickness. Regions I and II are studied in §3.2.1. Region III occurs where $\delta^*/\lambda^* = \mathcal{O}(1)$ and $\overline{x} = \mathcal{O}(1)$ and it is governed by the linearized unsteady boundary-region equations (Leib *et al.* 1999). In region IV, which is in the pipe core and surrounded by region III, the base flow is inviscid and the perturbation flow is viscous. Regions III and IV are discussed in §3.2.2. In region V the base flow is not self-similar because of the unknown pressure gradient. The streamwise base-flow velocity at the pipe axis increases with x and the base flow is non-parallel as the radial velocity plays a key role. The latter vanishes farther downstream in region VI, where the parabolic Poiseuille profile occurs.

2.2. *Governing equations and boundary conditions*

The flow field is governed by the continuity and Navier-Stokes equations,

$$\nabla \cdot \mathbf{u} = 0, \tag{2.3}$$

$$\frac{\partial \mathbf{u}}{\partial t} + (\mathbf{u} \cdot \nabla)\,\mathbf{u} = -\nabla p + \frac{1}{Re_\lambda}\nabla^2 \mathbf{u}, \tag{2.4}$$

where $\mathbf{u} = \{u_x, u_r, u_\theta\}$. The velocity $\mathbf{u}$ and the pressure p are expressed as the superposition of the base flow and the perturbation flow, i.e. $\{\mathbf{u}, p\} = \{\overline{\mathbf{U}}(\overline{x}, r), \overline{P}(\overline{x}) + \{\mathbf{u}', p'\}$, where

$$\left\{\overline{\mathbf{U}}(\overline{x}, r), \overline{P}(\overline{x})\right\} = \left\{U(\overline{x}, r), k_x V(\overline{x}, r), 0, P(\overline{x})\right\}, \tag{2.5}$$

$$\{\mathbf{u}', p'\} = \{u', v', w', p'\} = \varepsilon \begin{pmatrix} \overline{u}_{x,0}(\overline{x}, r) \\ \overline{u}_{r,0}(\overline{x}, r) \\ \overline{u}_{\theta,0}(\overline{x}, r) \\ \overline{p}_0(\overline{x}, r) \end{pmatrix} e^{i(m\theta - k_x t)} + \text{c.c.}, \tag{2.6}$$

and

$$\{\overline{u}_{x,0}, \overline{u}_{r,0}\} = \left\{\overline{u}_x^{(0)}, k_x \overline{u}_r^{(0)}\right\} + \left\{\frac{im}{k_x}\overline{u}_x, im\overline{u}_r\right\}, \tag{2.7a}$$

$$\overline{u}_{\theta,0} = -\frac{ik_x}{m}\overline{u}_\theta^{(0)} + \overline{u}_\theta, \tag{2.7b}$$

$$\overline{p}_0 = \frac{k_x}{Re_\lambda}\overline{p}^{(0)} + \frac{im}{Re_\lambda}\overline{p}. \tag{2.7c}$$

The notation in (2.6)-(2.7) is as close as possible to the flat-plate case by Leib *et al.* (1999) for ease of understanding. The main difference between $\overline{u}_r$ and $\overline{u}_r^{(0)}$ and the corresponding components in (4.1) on page 176 of Leib *et al.* (1999) is the missing factor $(2\overline{x})^{1/2}$ in (2.6), which arises in Leib *et al.* (1999)'s case because of the Blasius-similarity scaling.

By substituting (2.5)-(2.6) into (2.3)-(2.4) and collecting the terms of $\mathcal{O}(1)$, one obtains the base-flow boundary-layer equations (Hornbeck 1964),

$$\frac{\partial U}{\partial \overline{x}} + \frac{V}{r} + \frac{\partial V}{\partial r} = 0, \tag{2.8}$$

$$U\frac{\partial U}{\partial \overline{x}} + V\frac{\partial U}{\partial r} = -\frac{\mathrm{d}P}{\mathrm{d}\overline{x}} + \frac{1}{\mathcal{F}}\left(\frac{1}{r}\frac{\partial U}{\partial r} + \frac{\partial^2 U}{\partial r^2}\right), \tag{2.9}$$

$$\frac{\partial P}{\partial r} = 0, \tag{2.10}$$

for $k_x, Re_\lambda^{-1} \ll 1$ and $\mathcal{F} = k_x Re_\lambda = \mathcal{O}(1)$. As P is unknown, (2.8)-(2.9) are solved together with the mass conservation law, $\int_0^R Ur\,\mathrm{d}r = R^2/2$, found by averaging across a pipe cross-section. Equations (2.8)-(2.9) are subject to the no-slip and no-penetration conditions at the pipe wall, $U = V = 0$ at $r = R$, and to the symmetry conditions at the axis, $\partial U/\partial r = V = 0$ at $r = 0$. As p' at the wall is unknown, we eliminate the pressure from (2.3)-(2.4) (Kim *et al.* 1987) to obtain the perturbation-flow equations,

$$\widehat{V}\overline{u}_r + \widehat{V}_r\frac{\partial \overline{u}_r}{\partial r} + \widehat{V}_{rr}\frac{\partial^2 \overline{u}_r}{\partial r^2} + \widehat{V}_{rrr}\frac{\partial^3 \overline{u}_r}{\partial r^3} + \widehat{V}_{rrrr}\frac{\partial^4 \overline{u}_r}{\partial r^4} + \widehat{V}_x\frac{\partial \overline{u}_r}{\partial \overline{x}} + \widehat{V}_{xr}\frac{\partial^2 \overline{u}_r}{\partial \overline{x}\partial r} + \widehat{V}_{xrr}\frac{\partial^3 \overline{u}_r}{\partial \overline{x}\partial r^2} +$$
$$\widehat{U}\overline{u}_x + \widehat{U}_r\frac{\partial \overline{u}_x}{\partial r} + \widehat{U}_{rr}\frac{\partial^2 \overline{u}_x}{\partial r^2} + \widehat{U}_x\frac{\partial \overline{u}_x}{\partial \overline{x}} + \widehat{U}_{xr}\frac{\partial^2 \overline{u}_x}{\partial \overline{x}\partial r} + \widehat{U}_{xrr}\frac{\partial^3 \overline{u}_x}{\partial \overline{x}\partial r^2} = 0, \tag{2.11}$$

$$\left(-i + \frac{m^2}{\mathcal{F}r^2} + \frac{\partial U}{\partial \overline{x}}\right)\overline{u}_x + \left(V - \frac{1}{\mathcal{F}r}\right)\frac{\partial \overline{u}_x}{\partial r} + U\frac{\partial \overline{u}_x}{\partial \overline{x}} - \frac{1}{\mathcal{F}}\frac{\partial^2 \overline{u}_x}{\partial r^2} + \frac{\partial U}{\partial r}\overline{u}_r = 0, \tag{2.12}$$

The coefficients of (2.11) are

$$\widehat{V} = \left(\frac{1}{m^2} - 1\right)\left(\boxed{i} - \frac{\partial V}{\partial r} + \frac{1-m^2}{\mathcal{F}r^2}\right) + \frac{2r}{m^2}\frac{\partial^2 U}{\partial r\partial \overline{x}} + \frac{r^2}{m^2}\frac{\partial^3 U}{\partial r^2\partial \overline{x}} \tag{2.13}$$

$$\widehat{V}_r = \boxed{\frac{3ir}{m^2}} - \frac{3r}{m^2}\frac{\partial V}{\partial r} - \frac{1}{\mathcal{F}rm^2} - \frac{2}{\mathcal{F}r} + V - \frac{4V}{m^2} + \frac{r^2}{m^2}\frac{\partial^2 U}{\partial r\partial \overline{x}} \tag{2.14}$$

$$\widehat{V}_{rr} = \frac{1}{m^2}\left(\boxed{ir^2} - 5rV - r^2\frac{\partial V}{\partial r} - \frac{2m^2}{\mathcal{F}} + \frac{5}{\mathcal{F}}\right) \tag{2.15}$$

$$\widehat{V}_{rrr} = \frac{1}{m^2}\left(\frac{6r}{\mathcal{F}} - r^2 V\right) \tag{2.16}$$

$$\widehat{V}_{rrrr} = \frac{r^2}{\mathcal{F}m^2} \tag{2.17}$$

$$\widehat{V}_x = U - \frac{U}{m^2} + \frac{r}{m^2}\frac{\partial U}{\partial r} + \frac{r^2}{m^2}\frac{\partial^2 U}{\partial r^2} \tag{2.18}$$

$$\widehat{V}_{xr} = -\frac{3rU}{m^2} \tag{2.19}$$

$$\widehat{V}_{xrr} = -\frac{r^2 U}{m^2} \tag{2.20}$$

$$\widehat{U} = \frac{\partial V}{\partial \overline{x}} + \frac{2r}{m^2} \frac{\partial^2 U}{\partial \overline{x}^2} + \frac{r^2}{m^2} \frac{\partial^3 U}{\partial \overline{x}^2 \partial r} \tag{2.21}$$

$$\widehat{U}_x = -\frac{2}{\mathcal{F}r} + \frac{6r}{m^2} \frac{\partial U}{\partial \overline{x}} + \frac{2r^2}{m^2} \frac{\partial^2 U}{\partial \overline{x} \partial r} \tag{2.22}$$

$$\widehat{U}_r = \frac{r}{m^2} \frac{\partial V}{\partial \overline{x}} \tag{2.23}$$

$$\widehat{U}_{rr} = \frac{r^2}{m^2} \frac{\partial V}{\partial \overline{x}} \tag{2.24}$$

$$\widehat{U}_{xr} = \frac{2}{m^2} \left(\frac{1}{\mathcal{F}} - 2rV - r^2 \frac{\partial V}{\partial r} \right) \tag{2.25}$$

$$\widehat{U}_{xrr} = \frac{2r}{m^2 \mathcal{F}}. \tag{2.26}$$

The boxed terms in (2.13)-(2.15) pertain to the unsteadiness and are asymptotically smaller than the other terms in the low-frequency limit $\mathcal{F} \ll 1$. The procedure to obtain (2.11)-(2.12) is given in the Supplementary Material S2. Equations (2.11) and (2.12) are also satisfied by $\{\overline{u}_x^{(0)}, \overline{u}_r^{(0)}\}$. At the start of the analysis, equation (2.12) is the radial vorticity equation, but it reduces to the x-momentum equation because the leading-order contribution to the radial vorticity is given by $\overline{u}_x$ due to $k_x \ll 1$. Equations (2.11) and (2.12) are subject to

$$\overline{u}_x = \overline{u}_r = \frac{\partial \overline{u}_r}{\partial r} = 0 \tag{2.27}$$

at $r = R$ because of the no-slip condition at the pipe wall and the continuity equation (S2.5). The boundary conditions at $r = 0$ are

$$m = 1: \quad \overline{u}_x = 0, \quad \overline{u}_r' = 0, \quad \overline{u}_\theta' = 0, \tag{2.28}$$

$$m = 2: \quad \overline{u}_x = 0, \quad \overline{u}_r = 0, \quad \overline{u}_\theta = 0, \tag{2.29}$$

$$m > 2: \quad \overline{u}_x = 0, \quad \overline{u}_r = 0, \quad \overline{u}_r' = 0, \tag{2.30}$$

where the prime here indicates the derivative with respect to r. For $m = 1$, (2.11)-(2.12) are solved together with the continuity equation (S2.5) because $\overline{u}_\theta$ appears in (2.28). For $m = 2$, this complication is avoided by using $\overline{u}_r'' = 0$ instead of the last condition in (2.29). The behaviour of the perturbation flow near the pipe axis and the derivation of the boundary conditions is further discussed in the Supplementary Material S3. The same boundary conditions are found for $\overline{u}_x^{(0)}, \overline{u}_r^{(0)}, \overline{u}_\theta^{(0)}$. The azimuthal velocity component $\overline{u}_\theta$ and the pressure $\overline{p}$ are computed a posteriori from the continuity equation (S2.5) and the azimuthal momentum equation (S2.8).

The base-flow equations (2.8)-(2.9) and the perturbation equations (2.11)-(2.12) are parabolic and thus the specification of the appropriate initial conditions is of crucial importance. We have devoted great attention to the formulation of physically meaningful initial conditions for both the base flow and the perturbation flow. The initial base-flow velocity profile has usually been assumed uniform (Hornbeck 1964). We instead take into account the interaction between the oncoming flow and the pipe wall by deriving an asymptotic solution composed of the Blasius flow near the walls (inner solution) and the inviscid flow in the pipe core, distorted by the developing boundary layers (outer solution). The Supplementary Material S4 discusses the conditions under which the curvature effects can be neglected near the wall. The small-x base-flow asymptotic initial condition used to solve the base-flow equations (2.8)-(2.9) is described in §3.1.

Perturbation inflow conditions for open boundary-layer computations are often specified as the continuous spectrum of the Orr-Sommerfeld equations (Jacobs & Durbin

2001; Brandt *et al.* 2004) or by selecting optimal perturbations, as those obtained for the flat-plate case by Andersson *et al.* (1999) and Luchini (2000). As inflow conditions, Buffat *et al.* (2014) imposed optimal disturbances within one of the boundary layers near the entrance of a channel, while perturbations were absent in the inviscid core.

We prescribe initial conditions that are superposed on the inviscid core flow and match the oncoming vortical disturbances at $\overline{x} = 0$, given in (2.1). Like the base flow, these initial conditions are expressed as asymptotic composite solutions of a viscous inner solution within the boundary layer and an outer solution where the base flow is inviscid in the pipe core because we are interested in their entrainment of vortical disturbances that occupy the entire cross-plane near the pipe mouth. The initial condition is not imposed at $\overline{x} = 0$ because the radial base-flow velocity is singular there and because the flow field is governed by the full Navier-Stokes equations in the immediate surroundings of the inlet. Therefore, the initial conditions are imposed at a location $0 < \overline{x}_0 \ll 1$.

Section 3.2 presents results for the development of the perturbation flow at small-$\overline{x}$ locations where the base-flow pressure gradient is negligible. These flow fields are small-$\overline{x}$ asymptotic solutions of the flow in region V and can therefore be used as initial conditions to solve equations (2.11)-(2.12) along the pipe, where the base-flow streamwise pressure gradient is fully influential.

2.3. *Critical streamwise location for linear stability*

As we are interested in the spatial transient growth of vortical disturbances in the entrance region, a first step is to report, as a function of the Reynolds number, the streamwise locations where TS waves appear. Figure 2 shows the neutral stability locations x_c/R as a function of the Reynolds number $Re_R = R Re_\lambda = U_\infty^* R^*/\nu^*$ computed by Gupta & Garg (1981) (blue line) and da Silva & Moss (1994) (red circles). The entrance flow is linearly stable for $Re_R < 11000$ and the unstable region has a finite extent along the x direction as the flow is always linearly stable when it reaches the fully developed condition. We also show the experimental neutral points by Sarpkaya (1975), measured by introducing disturbances at fixed locations on the pipe wall by electromagnetic excitation. da Silva & Moss (1994) claimed that the disagreement may be due to the finite amplitude of Sarpkaya (1975)'s perturbations, which cannot be captured by the linear stability theory. We focus on Reynolds numbers in the range $1000 < Re_R < 10000$ (marked by the light grey area in figure 2), i.e. small enough for TS waves not to appear and large enough for algebraically growing perturbations or transition to turbulence to have been observed in experimental studies.

3. Initial flow development

In this section we discuss the theoretical and numerical results of the base and perturbation flows near the pipe entrance, where the effect of the pipe confinement is important, but the influence of the base-flow pressure gradient is negligible at leading order. This mathematical analysis is relevant because, through the asymptotic formulation, the physical flow features near the entrance are revealed and the flow evolution farther downstream inside the pipe can be computed. As explained at the end of §2, the results obtained in this section will indeed specify the appropriate initial conditions for the computation of the base and the perturbation flows in region V, where the dynamics is fully influenced by the streamwise pressure gradient.
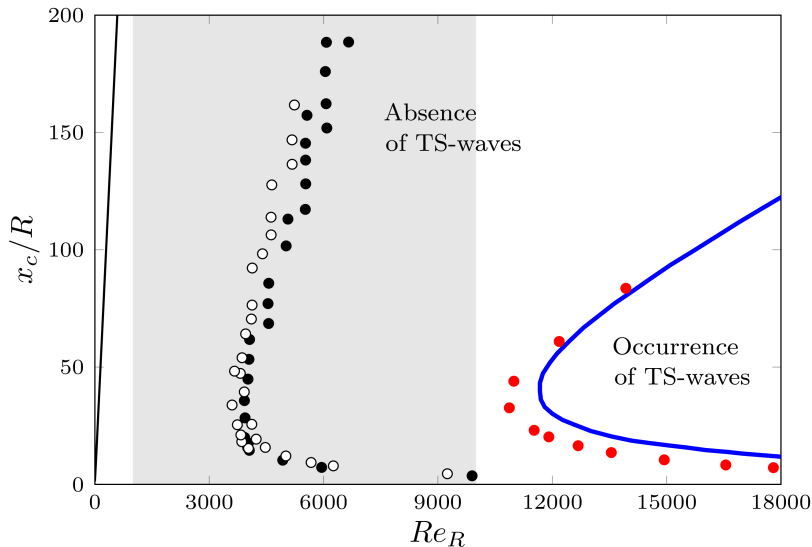
Figure 2: The blue line and red circles confine the unstable area according to classical stability theory, i.e. where TS waves start to grow, computed by Gupta & Garg (1981) and da Silva & Moss (1994), respectively. The black (axisymmetric disturbances) and white (non-axisymmetric disturbances) circles represent the experimental neutral points measured by Sarpkaya (1975). The solid black line denotes the end location of the entry pipe-flow region, according to our definition based on the second derivative of the base velocity at the centreline, discussed in §4.1. The grey area illustrates the range of Reynolds numbers for the flows studied.

3.1. *Initial base flow in regions I and II*

The initial base-flow solution is constructed according to the method of matched asymptotic expansions. The outer solution is the inviscid base flow in the core of the pipe, while the inner solution is the viscous flow attached to the pipe wall. The composite solution reads

$$\overline{\mathbf{U}} = \overline{\mathbf{U}}_{out} + \overline{\mathbf{U}}_{in} - \overline{\mathbf{U}}_{com}, \tag{3.1}$$

where the subscripts *in*, *out*, and *com* stand for inner, outer and common, respectively, and $\overline{\mathbf{U}}$ is defined in (2.5). The common part is defined as

$$\overline{\mathbf{U}}_{com} = \lim_{r \to R} \overline{\mathbf{U}}_{out} = \lim_{\eta \to \infty} \pm \overline{\mathbf{U}}_{in}, \tag{3.2}$$

where

$$\eta = (R - r) \left(\frac{Re_\lambda}{2x} \right)^{1/2} = \mathcal{O}(1) \tag{3.3}$$

is the scaled radial coordinate of the inner solution and in (3.2) the plus sign applies to the streamwise velocity and the minus sign applies to the radial velocity because the coordinates r and η point in opposite directions.

For the flow in the entrance region of a channel, the inner solution near the inlet corresponds to the Blasius flow as the Reynolds number is large (Wilson 1970; Rubin *et al.* 1977; Duck 2005; Buffat *et al.* 2014). We also benefit from the Blasius solution in the pipe-flow case as we have proved in the Supplementary Material S4 that the curvature effects are negligible near the wall. The inner flow therefore satisfies the self-similar

Blasius equation

$$F''' + FF'' = 0, \tag{3.4}$$

where the prime indicates differentiation with respect to η. The boundary conditions for equation (3.4) are $F(0) = 0$, $F'(0) = 0$ and $F' \to 1$ as $\eta \to \infty$. The inner base flow reads

$$\overline{U}_{in} = F', \quad \overline{V}_{in} = \frac{\eta F' - F}{(2xRe_\lambda)^{1/2}}. \tag{3.5}$$

As $Re_\lambda \gg 1$, the base-flow viscous effects are negligible in the pipe core near the entrance, which is consistent with the use of the boundary-layer approximation of the Navier-Stokes equations. In the pipe core, the axisymmetric outer flow is described by the inviscid Stokes stream function ψ,

$$\psi(x, r) = \frac{r^2}{2} + Re_\lambda^{-1/2} \psi_2(x, r), \tag{3.6}$$

i.e. $\overline{U}_{out} = r^{-1}\partial\psi/\partial r$ and $\overline{V}_{out} = -r^{-1}\partial\psi/\partial x$. The leading-order term $r^2/2$ in (3.6) represents the uniform streamwise flow. The second-order stream function ψ_2, which defines the flow due to the pipe confinement and to the Blasius boundary layer developing on the pipe wall, satisfies

$$\frac{\partial^2 \psi_2}{\partial x^2} + \frac{\partial^2 \psi_2}{\partial r^2} - \frac{1}{r}\frac{\partial \psi_2}{\partial r} = 0, \tag{3.7}$$

subject to

$$\psi_2 = \beta R\sqrt{2x} \quad \text{at} \quad r = R, x > 0 \tag{3.8a}$$

$$\psi_2 = 0 \quad \text{at} \quad r = R, x < 0 \tag{3.8b}$$

$$\psi_2 = 0 \quad \text{at} \quad r = 0, \tag{3.8c}$$

where $\beta = \lim_{\eta\to\infty}(\eta - F) = 1.217\ldots$. The inviscid base flow in the pipe core is irrotational and therefore the governing equation (3.7) is obtained by setting the azimuthal vorticity component to zero. Equation (3.7) is not the Laplace equation because of the negative sign of the last term (Panton 2013). The boundary condition (3.8a) is obtained by asymptotic matching, i.e. the radial component of the outer velocity must match the outer limit of the base-flow wall-normal velocity of the Blasius boundary layer,

$$\overline{V}_{com} = \lim_{r\to R}\overline{V}_{out} = \frac{-1}{RRe_\lambda^{1/2}}\frac{\partial\psi_2}{\partial x}\bigg|_{r=R} = -\lim_{\eta\to\infty}\overline{V}_{in} = \lim_{\eta\to\infty}\frac{F - \eta F'}{(2xRe_\lambda)^{1/2}} = \frac{-\beta}{(2xRe_\lambda)^{1/2}}, \tag{3.9}$$

where the minus sign in front of the η-limit is due to the inner and outer velocity components pointing towards opposite directions. It follows that

$$\psi_2(x) = \beta R \int (2x)^{-1/2}\mathrm{d}x = \beta R\sqrt{2x}, \tag{3.10}$$

at $r = R$ for $x > 0$. The boundary condition (3.8b) is obtained as follows. The base flow is uniform and streamwise only as $x \to -\infty$ and, as it is not influenced by the presence of the pipe, no wall-normal base-flow velocity occurs as $x \to -\infty$. Also, the horizontal line $r = R$ for $x < 0$ is a streamline with stagnation point at $x = 0^-, r = R$ and no wall-normal base-flow velocity occurs along it because the base flow approaches the pipe wall parallel to it. Therefore, $\overline{V}_{out} = 0$ at $r = R$ for $x < 0$, i.e. $\partial\psi/\partial x = \partial\psi_2/\partial x = 0$. As we choose $\psi_2 = 0$ as $x \to -\infty$, by integrating $\partial\psi_2/\partial x = 0$ from $x \to -\infty$ for $r = R$, it

follows that $\psi_2 = 0$ along $r = R$ for $x < 0$. The boundary condition (3.8*c*) follows from $\overline{V}_{out} = 0$ along the pipe axis at any x due to the flow axial symmetry.

The solution to (3.7) together with the boundary conditions (3.8) is found by use of the complex Fourier transform along x. The solution reads

$$\psi_2(x,r) = -\frac{r\beta i^{1/2}}{2\sqrt{2\pi}} \int_{-\infty+i\gamma}^{+\infty+i\gamma} \frac{I_1(\zeta r)e^{i\zeta x}}{I_1(\zeta R)\zeta^{3/2}} \mathrm{d}\zeta, \qquad (3.11)$$

where I_1 is the modified Bessel function of the first kind and $\gamma \in \mathbb{R} < 0$. The Supplementary Material S5 presents the derivation of (3.11) (Dettman 1965). The composite solution of the streamwise velocity U is

$$U(x,r) = \overline{U} = F'(\eta(x,r)) - \frac{\beta i^{1/2}}{2\sqrt{2\pi}Re_\lambda^{1/2}} \int_{-\infty+i\gamma}^{+\infty+i\gamma} \frac{e^{i\zeta x}}{\zeta^{1/2}I_1(\zeta R)} \left[\frac{I_1(\zeta r)}{\zeta r} + I_1'(\zeta r) \right] \mathrm{d}\zeta +$$

$$\frac{\beta i^{1/2}}{2\sqrt{2\pi}Re_\lambda^{1/2}} \int_{-\infty+i\gamma}^{+\infty+i\gamma} \frac{e^{i\zeta x}}{\zeta^{1/2}} \left[\frac{I_1'(\zeta R)}{I_1(\zeta R)} + \frac{1}{\zeta R} \right] \mathrm{d}\zeta.$$

$$(3.12)$$

The composite solution of the radial velocity V, defined in (2.5), is

$$V(x,r) = k_x^{-1}\overline{V} = \frac{\eta F'(\eta(x,r)) - F(\eta(x,r))}{k_x \left(2xRe_\lambda\right)^{1/2}} +$$

$$\frac{\beta i^{3/2}}{2\sqrt{2\pi}k_x Re_\lambda^{1/2}} \int_{-\infty+i\gamma}^{+\infty+i\gamma} \frac{I_1(\zeta r)e^{i\zeta x}}{I_1(\zeta R)\zeta^{1/2}} \mathrm{d}\zeta + \frac{\beta}{k_x \left(2xRe_\lambda\right)^{1/2}}.$$

$$(3.13)$$

Figure 3 shows the inner and outer solutions, their common parts, and the composite solutions for the base flow for $Re_\lambda = 500$ and 2000 at $x = 0.04$. The composite base-flow streamwise velocity, depicted in figure 3(a,b), agrees well with the inner Blasius solution across the pipe radius as the acceleration in the pipe core is still small at this x location. The increase of inviscid streamwise velocity balances the decrease within the viscous region to conserve the mass flow rate. The displacement effect of the Blasius boundary layers, given by (3.9), causes a small streamwise pressure gradient related to the dependence of the displacement stream function ψ_2 on the x coordinate. This small pressure gradient is negligible at leading order in the boundary layer. The inviscid streamwise velocity is larger than unity near the wall because it accelerates along x to conserve the mass flow rate as the radial velocity decreases from its boundary-layer blowing value as the pipe axis is approached. This acceleration gives rise to the local near-wall peak in the $\overline{U}$ profile, also reported in Durst *et al.* (2005) for entry-pipe flow and in Sparrow *et al.* (1964), Panton (2013) and Alizard *et al.* (2018) for entry-channel flows. The peak occurs because the inviscid streamwise velocity is larger than the viscous streamwise velocity deficit of the boundary layer.

The base-flow radial velocity, shown in figure 3(c,d), agrees well with the viscous solution only in the proximity of the wall, while the two fail to overlap in the inviscid core, where the composite profile coincides with the outer solution. The composite solution shows a distinct near-wall peak that moves closer to the wall and decreases in intensity as the Reynolds number increases. The velocity is not exactly zero at the wall. This small slip velocity decreases as $\mathcal{O}\left(Re_\lambda^{-1/2}\right)$ and induces a viscous layer at the next order, which is not computed.
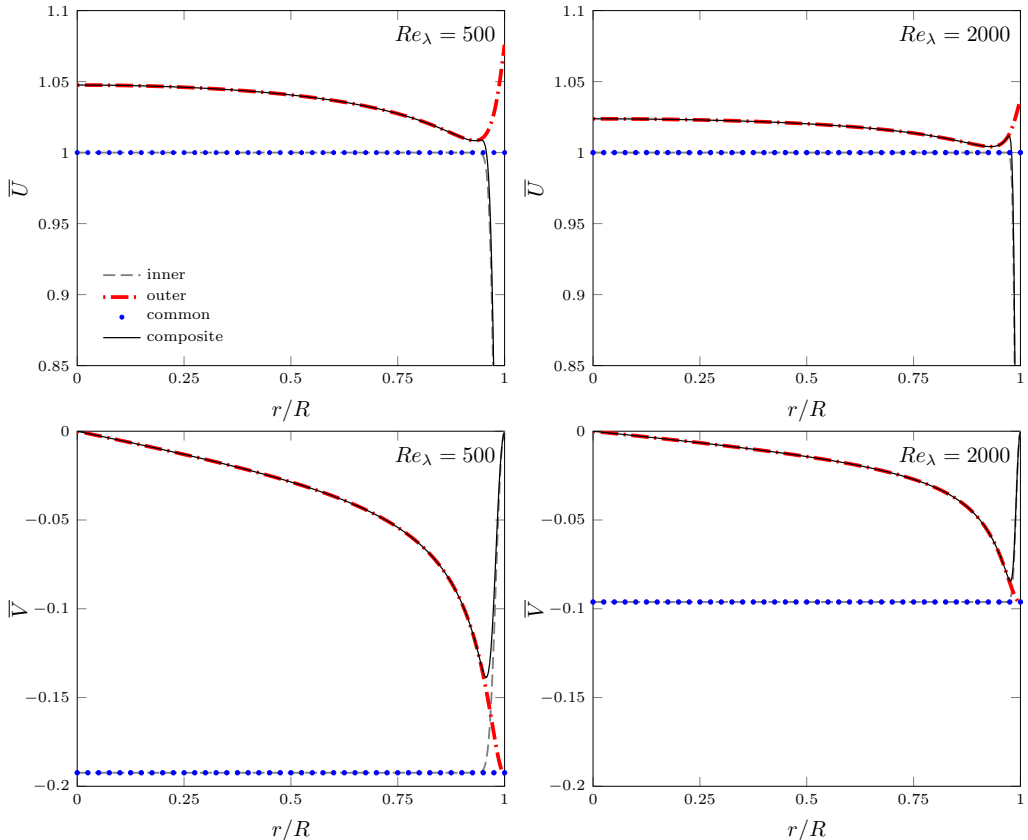
Figure 3: Composite solutions for the base-flow streamwise velocity $\overline{U}$ (top) and radial velocity $\overline{V}$ (bottom) at $x = 0.04$ for $R = 1$ and two Reynolds numbers.

3.2. *Initial perturbation flow*

The precise flow specification at the pipe entrance is relevant as our interest lies in the mathematical description of the inlet profiles to start the computations and to understand how the vortical disturbances are entrained in the pipe mouth and how they evolve in the entrance region. The initial perturbation flow, fully influenced by the confinement of the pipe and only mildly by the base-flow streamwise pressure, is studied in this section via matched asymptotic expansions. Asymptotic composite solutions are derived for regions I and II in §3.2.1. The flow in regions III and IV is discussed in §3.2.2.

3.2.1. *Perturbation flow in regions I and II*

In region I the base flow is uniform and inviscid, the perturbation flow is inviscid, and $\overline{x} \ll 1$ with $\mathcal{F} = \mathcal{O}(1)$. The flow field can thus be adequately described by rapid distortion theory (Goldstein 1978). The velocity is expressed as

$$\begin{aligned} \mathbf{u}_{out} =& \hat{\mathbf{i}} + \varepsilon \left[\mathbf{u}^{(1)}(\overline{x}, r) + k_x \mathbf{u}_1^{(1)}(\overline{x}, r) \right] e^{i(m\theta - k_x t)} + \text{c.c.} \\ =& \hat{\mathbf{i}} + \varepsilon \left(\mathbf{u}_\infty + \nabla\phi + k_x \nabla\phi_1 \right) + \text{c.c.}. \end{aligned} \tag{3.14}$$

The velocity $\mathbf{u}^{(1)}$ is due to the interaction of the free stream gust (2.1) with the pipe wall, while $\mathbf{u}_1^{(1)}$ is generated by the wall-normal boundary-layer perturbation velocity via

$\nabla\phi_1$. The perturbation potential ϕ satisfies the Laplace equation

$$\frac{1}{r}\frac{\partial}{\partial r}\left(r\frac{\partial\phi}{\partial r}\right) + \frac{1}{r^2}\frac{\partial^2\phi}{\partial\theta^2} + \frac{\partial^2\phi}{\partial x^2} = 0, \tag{3.15}$$

subject to

$$\phi \quad \text{finite} \quad \text{at} \quad r = 0, \tag{3.16a}$$

$$\frac{\partial\phi}{\partial r} + u_{\infty r} = 0 \quad \text{at} \quad r = R, \quad x > 0, \tag{3.16b}$$

where $u_{\infty r}(r = R) = \left[2\hat{u}_{r,mn}^{\infty}J_m(\xi_{mn}/2)/\xi_{mn}\right]\exp\left[ik_x(x-t)+im\theta\right]$ is the gust radial velocity found from (2.1) as the pipe wall is approached. Expression (3.16b) is the no-penetration boundary condition at the wall for the radial velocity. To solve (3.15) in the infinite strip $-\infty<x<\infty$, $0\leqslant r\leqslant R$, one needs a boundary condition at $r = R$ for $x < 0$, which is unknown. However, the interest here is in the solution at $x \gg 1$, which can be found by separation of variables. In this limit, it is found that $\phi = \hat{\phi}(r)\exp\left[ik_x(x-t)+im\theta\right]$, where $\hat{\phi}(r)$ satisfies the modified Bessel equation

$$r^2\frac{d^2\hat{\phi}}{dr^2} + r\frac{d\hat{\phi}}{dr} - \left(m^2 + k_x^2 r^2\right)\hat{\phi} = 0. \tag{3.17}$$

In the limit $k_x \ll 1$, the solution is

$$\phi = -\frac{2R\hat{u}_{r,mn}^{\infty}}{m\xi_{mn}}J_m\left(\frac{\xi_{mn}}{2}\right)\left(\frac{r}{R}\right)^m e^{[ik_x(x-t)+im\theta]}, \tag{3.18}$$

which is not singular when $m = 0$ because $\hat{u}_{r,0n}^{\infty} = 0$. Details of the derivation to obtain (3.18) are found in the Supplementary Material S6. The velocity components of $\mathbf{u}^{(1)} = \left\{u_x^{(1)}, u_r^{(1)}, u_\theta^{(1)}\right\}$ in (3.14) are

$$u_x^{(1)}(\overline{x},r) = u_{\infty x} + \frac{\partial\phi}{\partial x} = -\frac{2ik_x R\hat{u}_{r,mn}^{\infty}}{m\xi_{mn}}J_m\left(\frac{\xi_{mn}}{2}\right)\left(\frac{r}{R}\right)^m e^{i\overline{x}} + \hat{u}_{x,mn}^{\infty}J_m\left(\frac{\xi_{mn}r}{2R}\right)e^{i\overline{x}}, \tag{3.19}$$

$$u_r^{(1)}(\overline{x},r) = u_{\infty r} + \frac{\partial\phi}{\partial r} = -\frac{2e^{i\overline{x}}\hat{u}_{r,mn}^{\infty}}{\xi_{mn}}\left[J_m\left(\frac{\xi_{mn}}{2}\right)\left(\frac{r}{R}\right)^{m-1} - \frac{R}{r}J_m\left(\frac{\xi_{mn}r}{2R}\right)\right], \tag{3.20}$$

$$u_\theta^{(1)}(\overline{x},r) = u_{\infty\theta} + \frac{1}{r}\frac{\partial\phi}{\partial\theta} = -\frac{2i\hat{u}_{r,mn}^{\infty}}{\xi_{mn}}J_m\left(\frac{\xi_{mn}}{2}\right)\left(\frac{r}{R}\right)^{m-1}e^{i\overline{x}} - \frac{i\hat{u}_{\theta,mn}^{\infty}}{\xi_{mn}}J_m'\left(\frac{\xi_{mn}r}{2R}\right)e^{i\overline{x}}, \tag{3.21}$$

Using (2.6) and (2.7), the leading-order streamwise and radial velocities in region I are

$$\overline{u}_{x,out} = 0, \tag{3.22a}$$

$$\overline{u}_{r,out} = -\frac{iu_r^{(1)}}{m} = \frac{2ie^{i\overline{x}}\hat{u}_{r,mn}^{\infty}}{m\xi_{mn}}\left[J_m\left(\frac{\xi_{mn}}{2}\right)\left(\frac{r}{R}\right)^{m-1} - \frac{R}{r}J_m\left(\frac{\xi_{mn}r}{2R}\right)\right]. \tag{3.22b}$$

The leading-order azimuthal velocity $\overline{u}_{\theta,out} = u_\theta^{(1)}$ is given by (3.21) because of (2.7b). As the pipe wall is approached, $\overline{u}_{\theta,out}$ drives the inner flow in the viscous region II, where the azimuthal viscous diffusion effects do not play a leading role. As proved by the scaling in the Supplementary Material S4, the flow in region II is described by the unsteady boundary-layer equations in Cartesian coordinates because the curvature effects are

negligible near the wall. The inner solution for the radial velocity is $\overline{u}_{\theta,in} = \overline{u}_{\theta,com} F'(\eta)$, found by use of (4.13) in Leib *et al.* (1999), where the common part $\overline{u}_{\theta,com}$ is

$$\overline{u}_{\theta,com}(\overline{x}) = \overline{u}_{\theta,out}(r = R) = -\frac{ie^{i\overline{x}}}{\xi_{mn}} \left[2\hat{u}_{r,mn}^{\infty} J_m\left(\frac{\xi_{mn}}{2}\right) + \hat{u}_{\theta,mn}^{\infty} J_m'\left(\frac{\xi_{mn}}{2}\right) \right]. \quad (3.23)$$

The composite azimuthal velocity $\overline{u}_\theta$ is

$$\overline{u}_\theta = -\frac{2i\hat{u}_{r,mn}^{\infty}}{\xi_{mn}} J_m\left(\frac{\xi_{mn}}{2}\right)\left(\frac{r}{R}\right)^{m-1} e^{i\overline{x}} - \frac{i\hat{u}_{\theta,mn}^{\infty}}{\xi_{mn}} J_m'\left(\frac{\xi_{mn}r}{2R}\right) e^{i\overline{x}} + \overline{u}_{\theta,com}\left(F' - 1\right). \quad (3.24)$$

The solution (3.24) is not needed for the numerical computation in region V because $\overline{u}_\theta$ is absent from equations (2.11) and (2.12). However, the computation of $\overline{u}_{\theta,com}$ is essential because it determines the amplitude of the inner streamwise and radial velocities. The streamwise velocity component in region II is $\overline{u}_{x,in} = \overline{u}_{\theta,com}\overline{x}\eta F''/(2R)$. The $\overline{x}\eta F''/2$ dependence is found using (4.13) in Leib *et al.* (1999), and the amplitude $\overline{u}_{\theta,com}$ is obtained by converting the continuity equation from cylindrical to Cartesian coordinates and by taking the limit $r \to R$. As $\overline{u}_{x,out} = 0$, the composite streamwise velocity $\overline{u}_x$ is

$$\overline{u}_x = \overline{u}_{\theta,com} \frac{\overline{x}\eta F''}{2R}. \quad (3.25)$$

The asymptotic approach is clearly an invaluable tool as the amplitude of the streamwise perturbation velocity is uniquely linked to the oncoming free stream flow characteristics through $\overline{u}_{\theta,com}$, given in (3.23). Had the perturbation been prescribed within the boundary layer without relating to the oncoming fluctuations, the streak amplitude should have been assigned arbitrarily.

The composite radial velocity $\overline{u}_r$ is found by first summing the outer solution (3.22) and the inner solution obtained by multiplying the region-II wall-normal velocity (4.13) in Leib *et al.* (1999) by the amplitude $\overline{u}_{\theta,com}$ and by $(2\overline{x})^{1/2}$ on using (4.1) in Leib *et al.* (1999). The common part, i.e. the large-η limit of the region-II solution, is then subtracted. The common part also emerges from the second-order term of the Taylor expansion of the outer solution (3.22) as $r \to R$, while the leading-order term vanishes because of the no-penetration condition (3.16b). The composite radial velocity $\overline{u}_r$ is

$$\overline{u}_r = \underbrace{\frac{2ie^{i\overline{x}}\hat{u}_{r,mn}^{\infty}}{m\xi_{mn}} \left[J_m\left(\frac{\xi_{mn}}{2}\right)\left(\frac{r}{R}\right)^{m-1} - \frac{R}{r} J_m\left(\frac{\xi_{mn}r}{2R}\right) \right]}_{\text{outer solution}} - \\ \underbrace{\frac{\overline{u}_{\theta,com}}{4R}\left(\frac{2\overline{x}}{\mathcal{F}}\right)^{1/2}\left(\eta^2 F'' - 3\eta F' - F\right)}_{\text{inner solution}} - \underbrace{\frac{\overline{u}_{\theta,com}}{R}\left(\frac{2\overline{x}}{\mathcal{F}}\right)^{1/2}\eta}_{\text{common part}}. \quad (3.26)$$

The initial conditions for $\left\{\overline{u}_x^{(0)}, \overline{u}_r^{(0)}, \overline{u}_\theta^{(0)}\right\}$, defined in (2.7), are also found through a composite solution. The solution for the streamwise velocity $\overline{u}_x^{(0)}$ is found by combining the outer solution (3.19) and the inner solution given by (4.13) in Leib *et al.* (1999), valid for $\mathcal{F} = \mathcal{O}(1)$ and $\overline{x} \ll 1$. The composite streamwise velocity $\overline{u}_x^{(0)}$ is

$$\overline{u}_x^{(0)} = \hat{u}_{x,mn}^{\infty} J_m\left(\frac{\xi_{mn}r}{2R}\right) e^{i\overline{x}} + \hat{u}_{x,mn}^{\infty} J_m\left(\frac{\xi_{mn}}{2}\right) e^{i\overline{x}} \left[\frac{(\eta F')' + F'}{2} - 1 \right]. \quad (3.27)$$

The first term in (3.19) can be neglected because it is $\mathcal{O}(k_x)$. The inner solution for

the radial velocity $\overline{u}_r^{(0)}$ is found by (4.13) in Leib *et al.* (1999), which is also valid for $\mathcal{F} = \mathcal{O}(1)$ and $\overline{x} \ll 1$. It reads

$$\overline{u}_{r,in}^{(0)} = -\frac{\hat{u}_{x,mn}^{\infty} J_m\left(\xi_{mn}/2\right)}{2(2\overline{x}\mathcal{F})^{1/2}} \left[\eta(\eta F')' - F\right]. \tag{3.28}$$

Physically this perturbation velocity represents a radial blowing/suction effect, an unsteady analogue to the one experienced by the base-flow Blasius boundary layer. In the Blasius case, the base wall-normal velocity is generated by the free stream uniform U_∞^*, while $\overline{u}_{r,out}^{(0)}$ is driven by $\overline{u}_{x,out}^{(0)}$. The transpiration velocity induces the inviscid velocity field $\mathbf{u}_1^{(1)}$ in (3.14) and the associated radial pressure gradient. The velocity potential ϕ_1 satisfies

$$\nabla^2 \phi_1 = 0, \tag{3.29}$$

subject to

$$\phi_1 \quad \text{finite} \quad \text{at} \quad r = 0, \tag{3.30a}$$

$$\frac{\partial \phi_1}{\partial r} = \lim_{\eta \to \infty} \overline{u}_{r,in}^{(0)} = -\beta \frac{\hat{u}_{x,mn}^{\infty} J_m\left(\xi_{mn}/2\right)}{2(2\overline{x}\mathcal{F})^{1/2}} e^{im\theta - ik_x t} \quad \text{at} \quad r = R, \quad x > 0, \tag{3.30b}$$

Similar to the problem of solving (3.15), (3.29) cannot be solved in the infinite strip $-\infty < x < \infty$, $0 \leqslant r \leqslant R$ because the boundary condition at $r = R$ for $x < 0$ is unknown. In our region of interest, $x \gg 1$, the second derivative of ϕ_1 with respect to x is asymptotically smaller than the other derivatives as long as $k_x \ll \overline{x} \ll 1$ because of the $(2\overline{x})^{-1/2}$ behaviour of the boundary conditions (3.30b). By separating the variables and expressing $\phi_1 = \hat{\phi}_1(r) \exp\left(im\theta - ik_x t\right)/(2\overline{x})^{1/2}$, equation (3.29) simplifies to the Euler differential equation. The solution is

$$\hat{\phi}_1 = -\beta \frac{\hat{u}_{x,mn}^{\infty} J_m(\xi_{mn}/2) r^m}{2m R^{m-1} \mathcal{F}^{1/2}}. \tag{3.31}$$

The composite radial velocity $\overline{u}_r^{(0)}$ reads

$$\overline{u}_r^{(0)} = -\frac{\hat{u}_{x,mn}^{\infty} J_m(\xi_{mn}/2)}{2(2\overline{x}\mathcal{F})^{1/2}} \left\{\eta(\eta F')' - F + \beta\left[\left(\frac{r}{R}\right)^{m-1} - 1\right]\right\}. \tag{3.32}$$

It is verified that $k_x \overline{u}_r^{(0)}$ is asymptotically smaller than $im\overline{u}_r$ and $\overline{u}_x^{(0)}$ where $k_x/Re_\lambda \ll \overline{x} \ll 1$, as required by the expansion (2.7). Differently from the leading-order components where $\overline{u}_{\theta,out}$ is needed to determine the amplitude of $\{\overline{u}_{x,in}, \overline{u}_{r,in}\}$, it is not necessary to compute $\overline{u}_{\theta,out}^{(0)}$ as we have already found $\{\overline{u}_x^{(0)}, \overline{u}_r^{(0)}\}$ to start the integration of the boundary-region equations (2.11) and (2.11).

Figures 4, 5, 6 and 7 show velocity profiles for different m and n values. The flow parameters have been chosen as representative of the most significant cases, i.e. azimuthal wavelengths at $r = R$ and characteristic radial length scale comparable with the radius, Reynolds number with a middle value in the range of interest given in figure 2, and sufficiently small $\overline{x}$ for the asymptotic solutions to be valid.

In figures 4 and 5, increasing n causes the velocity profiles that are directly driven by the free stream forcing (2.1), i.e. $\overline{u}_r$, $\overline{u}_\theta$ and $\overline{u}_x^{(0)}$, to have a more intense modulation along the radial coordinate because the Bessel-function zeros ξ_{mn}, which appear in the argument of the Bessel functions in (2.1), increase in amplitude. The zeros ξ_{mn} can thus be interpreted as analogous to wall-normal wavenumbers in the Cartesian geometry. Figures 4(c,d) and 6(c,d) show how the inner profiles (region II) and the outer profiles
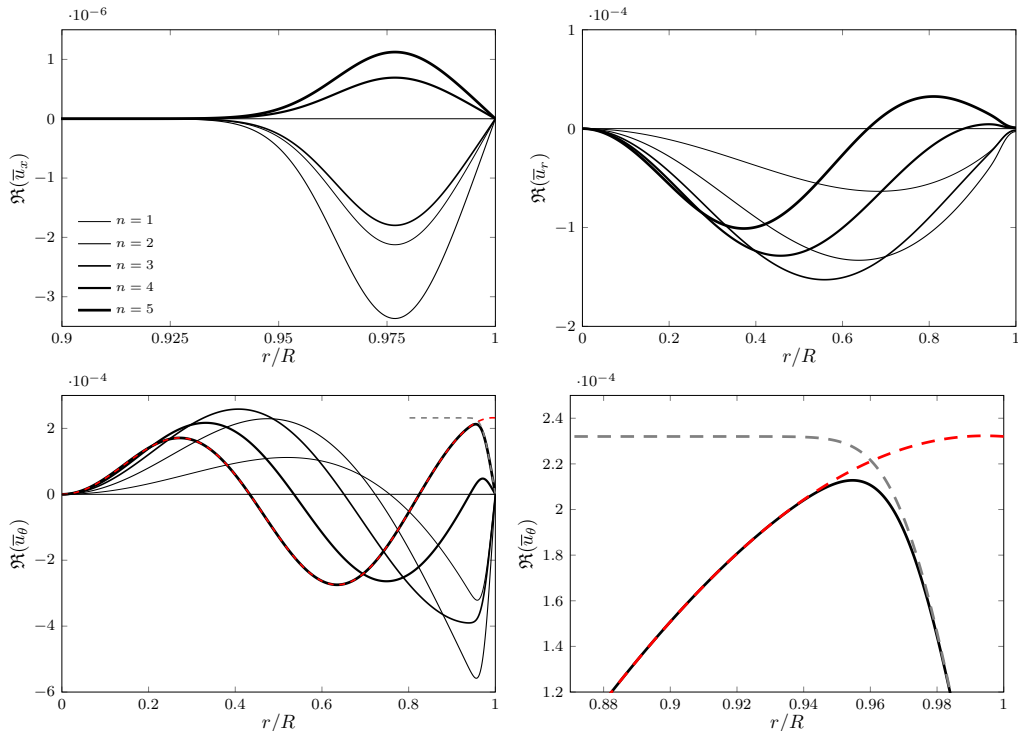
Figure 4: Real parts of composite velocities $\overline{u}_x$, $\overline{u}_r$, $\overline{u}_\theta$ in regions I and II for different n values and $m = 3$, $\overline{x} = 0.018$, $Re_\lambda = 4712$, $k_x = 0.37$, $R = 0.812$. In this figure and in figure 6, panel (d) shows a zoomed view of the asymptotic matching of the inner solution (dashed grey line) and the outer solution (dashed red line) of $\Re(\overline{u}_\theta)$.
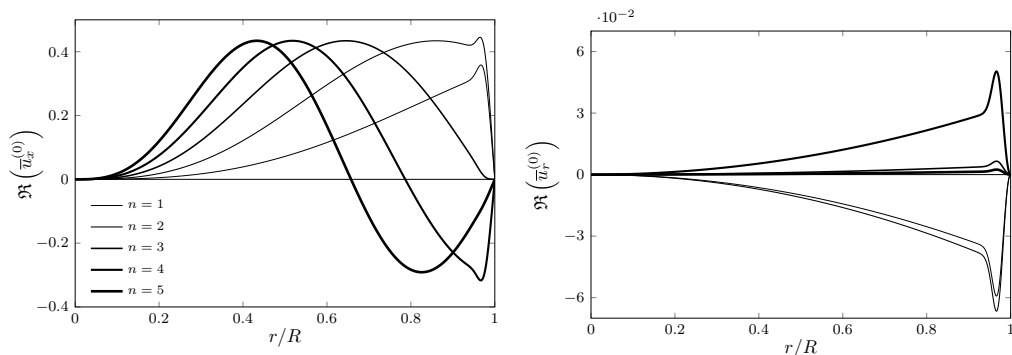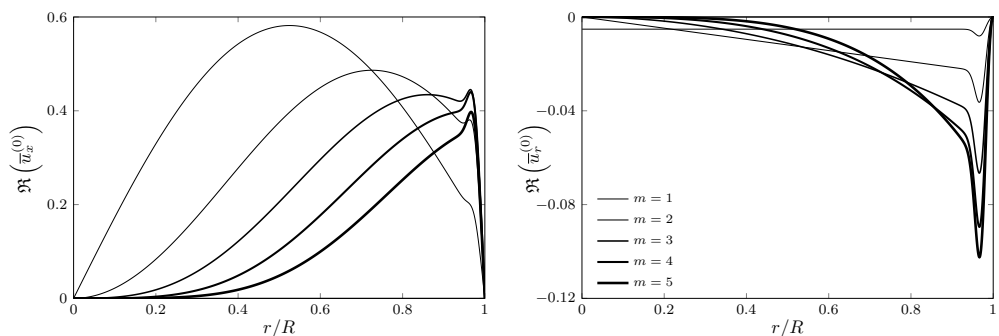

Figure 5: Real parts of composite velocities $\overline{u}_x^{(0)}$, $\overline{u}_r^{(0)}$ in regions I and II for different n values and $m = 3$, $\overline{x} = 0.018$, $Re_\lambda = 4712$, $k_x = 0.37$, $R = 0.812$.

(region I) of the azimuthal velocities combine to create the composite profiles valid at any radial location. Figure 8 shows contour plots of the composite velocity components and the pressure at a fixed time instant in a cross-plane near the pipe mouth.

The composite solutions (3.25)-(3.27) and (3.32) for $\overline{u}_x, \overline{u}_r, \overline{u}_x^{(0)}$, and $\overline{u}_r^{(0)}$ in regions I and II are used as initial conditions for the computation in regions V and VI.
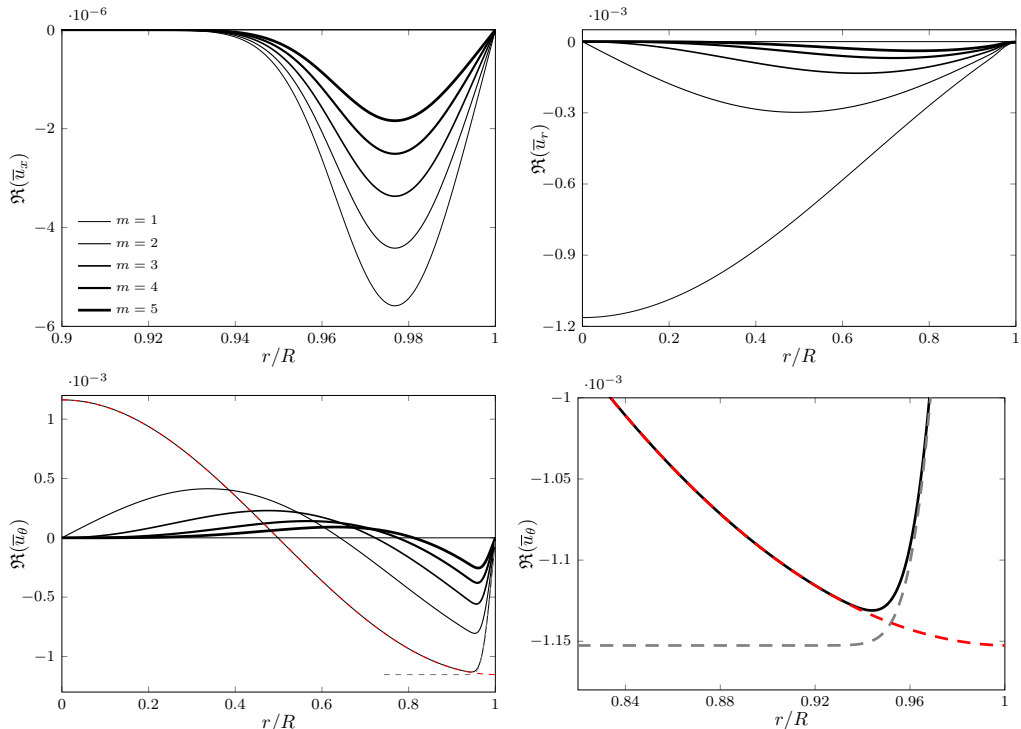
Figure 6: Real parts of composite velocities $\overline{u}_x$, $\overline{u}_r$, $\overline{u}_\theta$ in regions I and II for different m values and $n = 2$, $\overline{x} = 0.018$, $Re_\lambda = 4712$, $k_x = 0.37$, $R = 0.812$.

Figure 7: Real parts of composite velocities $\overline{u}_x^{(0)}$, $\overline{u}_r^{(0)}$ in regions I and II for different m values and $n = 2$, $\overline{x} = 0.018$, $Re_\lambda = 4712$, $k_x = 0.37$, $R = 0.812$.

3.2.2. *Perturbation flow in regions III and IV*

The outer expressions (3.22) do not take into account the viscous decay as they are only valid in the inviscid region I, i.e. for $\overline{x} \ll 1$. Viscous effects become important as the outer flow evolves downstream through region IV. The flow in regions III and IV can be found by a composite solution. The expression for the outer velocity field in region IV can be written as

$$\mathbf{u} = \left\{ \frac{1}{r}\frac{\partial \psi}{\partial r}, -\frac{1}{r}\frac{\partial \psi}{\partial x}, 0 \right\} + \varepsilon \mathbf{u}_{out} e^{i(m\theta - k_x t)} + \text{c.c.}, \quad (3.33)$$
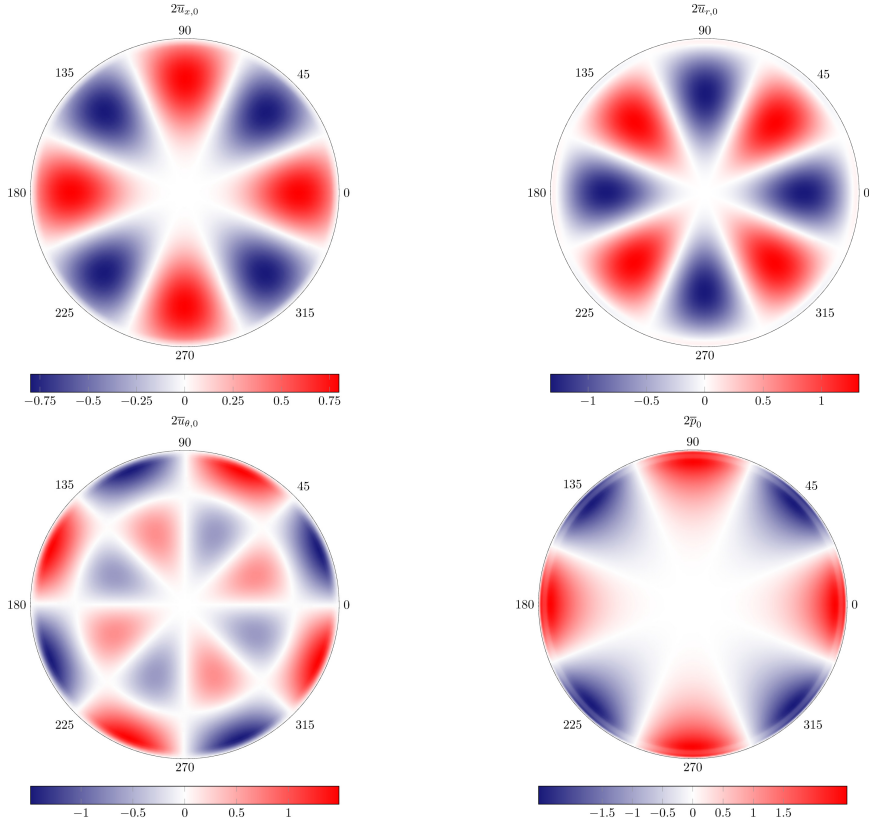
Figure 8: Contours of the instantaneous velocity components $2\overline{u}_{x,0}, 2\overline{u}_{r,0}, 2\overline{u}_{\theta,0}$ and pressure $2\overline{p}_0$ at $t = 0$, $\overline{x} = 0.018$, for $Re_\lambda = 2356$, $k_x = 0.185$, $R = 0.6366$ ($n = 3, m = 4$).

where the stream function $\psi(x, r)$ is given in (3.6) and (3.11). As depicted in figure 1, the base-flow pressure gradient only has a second-order effect through the x-dependence of $\psi(x, r)$. In the Cartesian geometry the outer velocity $\mathbf{u}_{out}$ can be obtained analytically by solving the parabolic region-IV momentum equation (5.9) on page 181 in Leib *et al.* (1999). In the cylindrical geometry, the radial and the azimuthal momentum equations are instead coupled and the system has to be solved numerically. The inner solution must also found numerically by solving the boundary-region equations (5.2)-(5.5) on page 180 of Leib *et al.* (1999), complemented by mixed-type boundary conditions obtained by asymptotically matching with the outer solution (3.33). These numerical calculations are not pursued herein because our region-V solution includes the solutions of regions III and IV and covers the whole streamwise flow evolution as the base-flow pressure gradient is accounted for at leading order.

4. Downstream flow development

In §3 the base and perturbation flows are influenced by the confinement of the pipe, but the streamwise location is sufficiently upstream for the base-flow streamwise pressure gradient not to play a leading-order role. In the present section, we consider region V, i.e. streamwise locations where the base-flow pressure gradient instead plays a leading-order role on the base flow and therefore on the perturbation flow. In region VI, the pressure gradient adjusts downstream to a constant value as the base flow develops to the fully developed Poiseuille flow. The base-flow profiles are obtained by solving (2.8)-(2.9) and the perturbation profiles are found by solving (2.11)-(2.12).

4.1. *Base flow*

The base-flow streamwise and wall-normal velocity profiles across the pipe are shown in figure 9 at different streamwise positions. The small-x asymptotic profiles (3.1) are also shown (dashed lines). The flow field approaches the fully developed regime as it develops downstream: the base-flow streamwise velocity evolves to the parabolic Poiseuille profile, while the wall-normal velocity decreases to zero.

The base-flow streamwise velocity is shown in figure 10 at various r/R locations as a function of the streamwise position. There is excellent agreement with the numerical data by Hornbeck (1964) (red circles) and very good agreement with the experimental data by Reshotko (1958) (white circles), except at the two locations closest to the pipe wall, where the uncertainty of the measurements may have been influential.

The downstream adjustment of the pressure gradient can be monitored through the correction pressure function

$$\mathcal{K}\left(\frac{x}{R^2 Re_\lambda}\right) = \frac{|\Delta\overline{P}^*|}{\rho^* U_\infty^{*2}} - \frac{8\nu^* x^*}{R^{*2} U_\infty^*} = |\Delta\overline{P}| - \frac{8x}{R^2 Re_\lambda}, \tag{4.1}$$

which measures the deviation of the base-flow pressure, defined in (2.5), from the fully developed Poiseuille value. Our numerical data, shown in figure 11, agree well with the numerical data based on the series solution by Sparrow *et al.* (1964) (red circles) and satisfactorily with the experimental data by Mohanty & Asthana (1978). Our fully developed computed value, $\mathcal{K}_\infty = \lim_{x\to\infty}\mathcal{K}(x) = 0.63$, matches the one by Sparrow *et al.* (1964) and is slightly lower than the experimental values by Shapiro *et al.* (1954) (square) and Knibbs (reported by Sparrow *et al.* (1964), triangle).

We can define boundary-layer thicknesses to quantify the diffusion of the viscous effects as the flow develops downstream. They are defined as

$$\delta_k = \Delta_k \int_0^R \left[1 - \frac{\overline{U}(x,r)}{\overline{U}_{\mathrm{cen}}(x)}\right] \mathrm{d}r, \tag{4.2}$$

where $k = R$ identifies the boundary thickness that matches the pipe radius in the fully developed downstream limit ($\Delta_R = 3$ is obtained by substituting $\delta_R = R$, $\lim_{x\to\infty}\overline{U}(x,r) = 2[1 - (r/R)^2]$, and $\lim_{x\to\infty}\overline{U}_{\mathrm{cen}} = 2$ into (4.2)) and $k = \mathrm{LWG,PIPE}$ denotes the boundary thickness that matches the one employed by Leib *et al.* (1999) as $x \to 0$, i.e. $\delta_{\mathrm{LWG}} = (2x/Re_\lambda)^{1/2}$ ($\Delta_{\mathrm{LWG,PIPE}} = \beta^{-1} = 0.822$ is obtained by substituting (3.12) into (4.2)). Figure 12 (left) shows the boundary-layer thicknesses as functions of the streamwise coordinate. The thickness $\delta_{\mathrm{LWG,PIPE}}$ in our pipe-flow flow case is thinner than the corresponding Blasius-flow δ_{LWG} because of the accelerating core caused by the favourable pressure gradient.

We also quantify the entry length, i.e. the distance from the pipe mouth where region V ends and the fully developed region VI starts. The entry length is typically
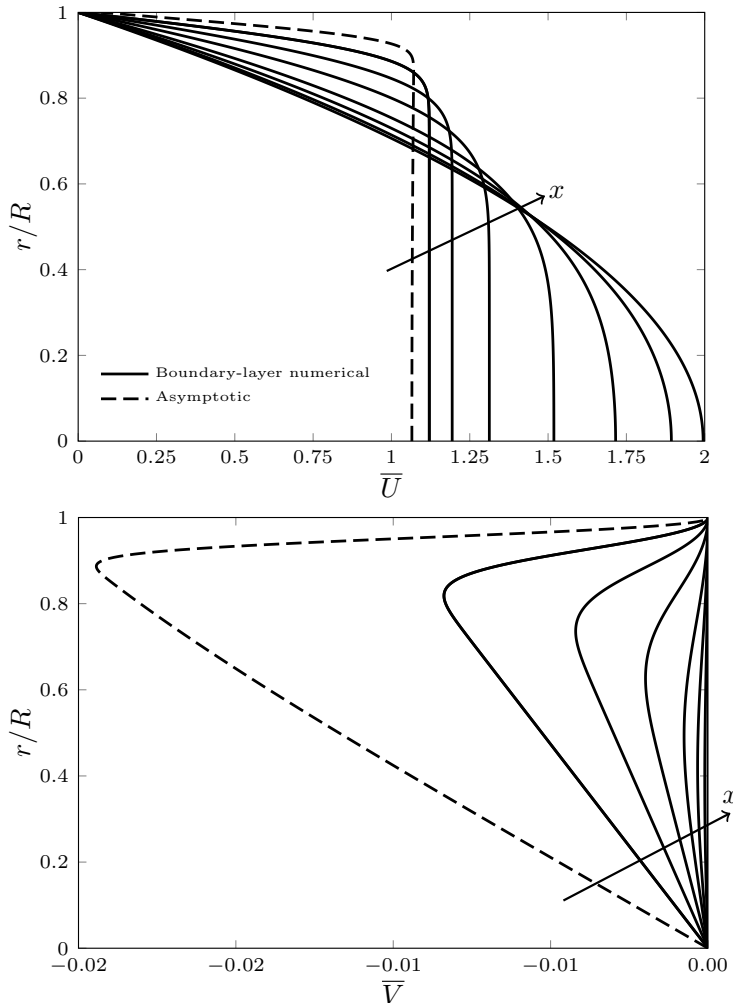
Figure 9: Streamwise (top) and wall-normal (bottom) base-flow velocity profiles. The solid lines denote the solutions at $x/(R^2 Re_\lambda) = 0.0012, 0.0036, 0.01, 0.03, 0.06, 0.12, 0.6$ obtained by numerically solving the boundary-layer equations (2.8)-(2.9). The dashed lines show the composite solution of the streamwise velocity (3.12) (top) and of the wall-normal velocity (3.13) (bottom) at $x/(R^2 Re_\lambda) = 0.0004$.

defined by the streamwise location where the axis base velocity $\overline{U}_{\mathrm{cen}}$ reaches 99% of its fully developed value. We can first use equation (23) in Durst *et al.* (2005), i.e. $x_{e,u} = 2R \left[0.4642 + (2C_{e,u} R Re_\lambda)^{1.6} \right]^{1/1.6}$, where $C_{e,u} = 0.0567$. As we operate under the assumption $Re_\lambda \gg 1$, Durst *et al.* (2005)'s equation reduces to $x_{e,u} = 4C_{e,u} R^2 Re_\lambda$, which is consistent with the scaling adopted in figure 10. We compute $C_{e,u} = 0.057$, which is within the uncertainty range provided by Durst *et al.* (2005). We also quantify the entrance region as $x_{e,pres} = 4C_{e,pres} R^2 Re_\lambda$, i.e. the streamwise distance from the pipe mouth where $\mathcal{K} = 0.99 \mathcal{K}_\infty$, that is, where the pressure gradient has reached its fully developed constant value. We compute $C_{e,pres} = 0.055$.

Crabtree, Küchemann & Sowerby on page 440 of Rosenhead (1963) remark that in a pipe entrance flow:'...the whole of the fluid across a section becomes influenced by viscosity before the parabolic profile is reached.' We can examine this statement, although
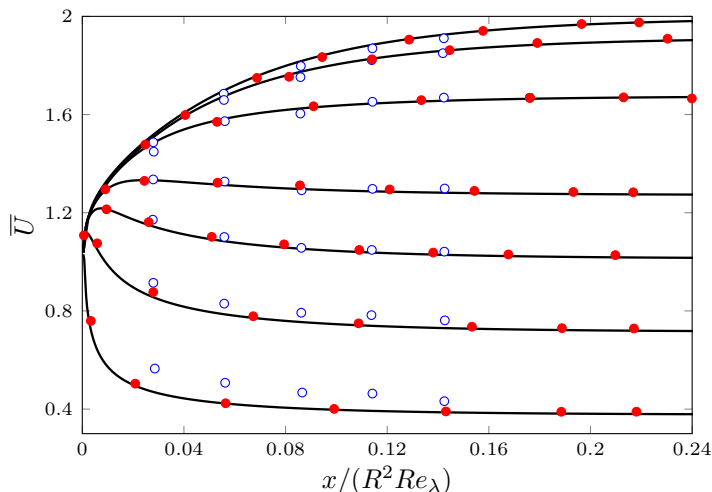
Figure 10: Base-flow streamwise velocity $\overline{U}$ at $r/R = 0, 0.2, 0.4, 0.6, 0.7, 0.8, 0.9$ (from top to bottom) as a function of the streamwise coordinate, computed by numerically solving the boundary-layer equations (2.8)-(2.9) (solid lines). The symbols are experimental data by Reshotko (1958) (empty circles) and boundary-layer numerical data by Hornbeck (1964) (red circles).
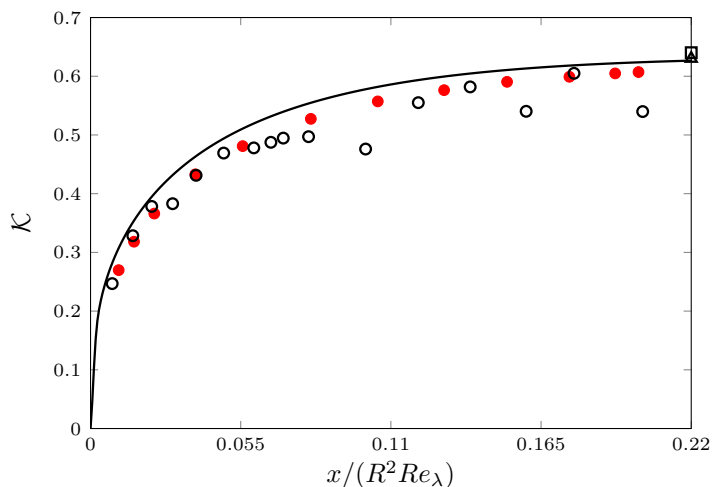

Figure 11: Correction pressure function $\mathcal{K}$, defined in (4.1), as a function of the streamwise coordinate, computed by numerically solving the boundary-layer equations (2.8)-(2.9) (solid line). The symbols are numerical data by Sparrow *et al.* (1964) (red circles) and experimental data by Mohanty & Asthana (1978) (white circles), Shapiro *et al.* (1954) (square) and Knibbs (reported by Sparrow *et al.* (1964), triangle).

they do not specify how the diffusion of viscous effects is defined mathematically. The development of the flow to the Poiseuille parabolic profile is already quantified by the entry length $x_{e,u}$, based on the downstream evolution of $\overline{U}_{\text{cen}}$, but we also further monitor it by an adjustment length $x_{e,pois} = 4C_{e,pois}R^2 Re_\lambda$, defined as the streamwise location where the average difference between the streamwise velocity and the Poiseuille velocity, i.e. $\mathcal{E}(x) = R^{-1} \int_0^R |\overline{U}(x,r) - 2[1 - (r/R)^2]| \mathrm{d}r$ (shown by the dashed line in figure 12, right), has decayed to 1% of $\lim_{x\to 0} \mathcal{E} = 2/3$. We find $C_{e,pois} = 0.057$, i.e. the same as
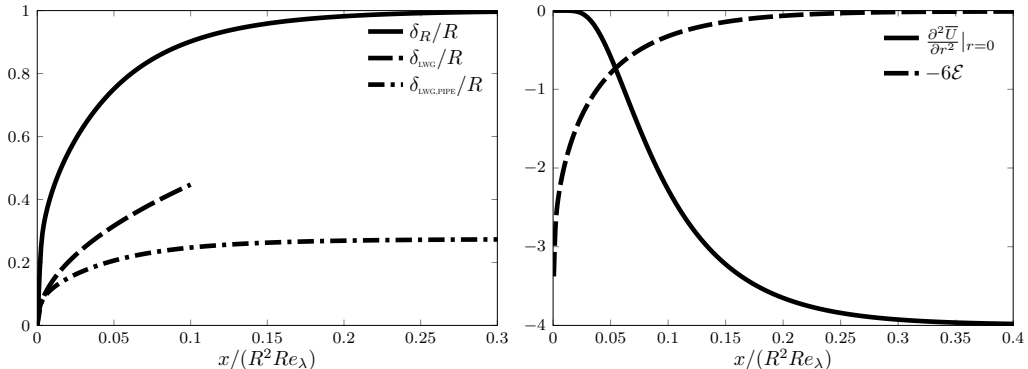
Figure 12: Left: Boundary-layer thicknesses δ_R, δ_{LWG} and $\delta_{\text{LWG,PIPE}}$ as functions of the streamwise coordinate. Right: Second derivative of the streamwise velocity at the pipe axis and average error $\mathscr{E}$, defined in the text and measuring the deviation of the $\overline{U}$ profile from the Poiseuille solution, as functions of the streamwise coordinate.

Criterion	$\mathrm{d}\overline{P}/\mathrm{d}\overline{x}$	$\mathscr{E}$	$\overline{U}_p(r=0)$	δ_R	$\left.\frac{\partial^2 \overline{U}}{\partial r^2}\right|_{r=0}$
Parameter	$C_{e,pres}$	$C_{e,pois}$	$C_{e,u}$	$C_{e,\delta}$	$C_{e,u2}$
	0.055	0.057	0.057	0.059	0.085
Entry length	$x_{e,pres}/(R^2 Re_\lambda)$	$x_{e,pois}/(R^2 Re_\lambda)$	$x_{e,u}/(R^2 Re_\lambda)$	$x_{e,\delta}/(R^2 Re_\lambda)$	$x_{e,u2}/(R^2 Re_\lambda)$
	0.219	0.228	0.226	0.237	0.341

Table 1: Entrance lengths according to the definitions in the text.

$C_{e,u}$. The diffusion of viscous effects can be quantified by two adjustment lengths. We first obtain $x_{e,u2} = 4C_{e,u2}R^2 Re_\lambda$, i.e. the downstream distance from the pipe mouth where the second derivative of the streamwise velocity with respect to the radial coordinate at the pipe axis, $\partial^2 \overline{U}/\partial r^2|_{r=0}$ (shown by the solid line in figure 12, right), is 99% of its fully developed value. We choose this quantity because it represents radial viscous effects and the axis is the last radial location where the viscous diffusion from the wall is felt. We compute $C_{e,u2} = 0.085$. We then find $x_{e,\delta} = 4C_{e,\delta}R^2 Re_\lambda$, i.e. the downstream distance from the entrance where δ_R=0.99R, and obtain $C_{e,\delta} = 0.059$. Table 1 summarizes the computed entrance lengths.

We therefore find that $C_{e,u2}$, $C_{e,\delta}$>$C_{e,u}, C_{e,pois}$, i.e. the flow becomes viscous for the whole wall-normal extent of the pipe slightly downstream from where the flow can be considered in good agreement with the Poiseuille profile. Therefore, there does not exist a distinct streamwise region along which viscous diffusion affects the whole wall-normal extent of the pipe and the velocity profile has not yet developed to the parabolic profile, which appears to be in contradiction with the statement by Crabtree, Küchemann & Sowerby. The adjustment length $x_{e,u2}$, based on the second wall-normal derivative of the streamwise velocity at the pipe axis, is the most conservative amongst the four lengths, as also visually evident in figure 12 (right).

Fluid	U_∞^* [m s^{-1}]	ν^* [m^{2}s^{-1}] $\times 10^6$	Re_∞^* [m^{-1}] $\times 10^{-3}$	R^* [m] $\times 10^3$	λ^* [m] $\times 10^3$	λ_x^* [m]	Re_λ	k_x	Re_R	λ_{xR}
Water	0.1	1	100	15	23.6	0.8	2356	0.185	1500	53.3
Air	1.3	13	100	15	23.6	0.8	2356	0.185	1500	53.3

Table 2: Parameters for water and air pipe flow experiments. The unit Reynolds number is $Re_\infty^* = U_\infty^*/\nu^*$ and $m = 4$.

4.2. *Perturbation flow*

The downstream evolution of the perturbation flow is discussed in this section. The scaling adopted in §2, which leads to $\overline{\mathbf{u}}_{\mathbf{x},0} = \overline{\mathbf{u}}_{\mathbf{x},0}(\overline{x}, r; Re_\lambda, k_x, n, m, R, \hat{u}_x^\infty, \hat{u}_r^\infty)$, is useful for the asymptotic analysis and it relates directly to the open-boundary-layer case of Leib *et al.* (1999). However, it is does not convey an immediate physical meaning as, for example, the scaled frequency k_x appears as an independent variable and in the scaling of $\overline{x}$. We therefore express the solution as $\overline{\mathbf{u}}_{\mathbf{x},0} = \overline{\mathbf{u}}_{\mathbf{x},0}(x_R, r_R; Re_R, \lambda_{xR}, n, \lambda_R, \hat{u}_x^\infty, \hat{u}_r^\infty)$, where the subscript R indicates scaling by the pipe radius R^*, i.e. $\lambda_R = \lambda^*/R^*$. In the cylindrical geometry, varying the index n allows studying the role of radial length scale, i.e. the larger n, the smaller the radial length scale.

In the analysis, we fix $\hat{u}_{x,mn}^\infty = 1$, and the kinetic energy of the gust at the pipe mouth, defined as

$$\mathcal{E}_{gust,R} = \frac{\mathcal{E}_{gust}^*}{U_\infty^{*2} R^{*2}} = \pi \int_0^1 \left(|u_{g,x}|^2 + |u_{g,r}|^2 + |u_{g,\theta}|^2\right) r_R \mathrm{d}r_R, \qquad (4.3)$$

(where $r_R = r^*/R^*$), is kept equal to $\mathcal{E}_{gust,11}$, the energy for $m = n = 1$ and $\hat{u}_{r,11}^\infty = 1$ ($u_{g,x}, u_{g,r}, u_{g,\theta}$ are the amplitudes of the free stream gust velocity components, defined in (2.1)). Expression (4.3) is written explicitly as

$$\mathcal{E}_{gust,R} = \pi \int_0^1 \left[r_R \left(\hat{u}_{x,mn}^\infty J_m\left(\overline{r}\right)\right)^2 + \frac{\left(4\hat{u}_{r,mn}^\infty J_m\left(\overline{r}\right)\right)^2}{r_R \xi_{mn}^2} + r_R \frac{\left(\hat{u}_{r,mn}^\infty J_m'\left(\overline{r}\right)\right)^2}{m^2}\right] \mathrm{d}r_R,$$

$$\qquad (4.4)$$

where $\overline{r} = \xi_{mn} r_R/2$ and $\hat{u}_{\theta,mn}^\infty$ has been eliminated by using (2.2). Setting $\mathcal{E}_{gust} = \mathcal{E}_{gust,11}$ allows computing $\hat{u}_{r,mn}^\infty$ for m, n of choice and use of (2.2) gives $\hat{u}_{\theta,mn}^\infty$.

We first study the velocity and pressure profiles of a reference case that is representative of realistic water and air pipe-flow experiments. Table 2 presents the flow parameters of these cases. We then study the effect of the inflow parameters on the perturbation field.

4.2.1. *Initial reference-case flow*

The region-I-II asymptotic initial conditions require a smooth matching with the numerical solutions of the boundary-region equations (2.11) and (2.12) at small x_R locations. This matching is monitored by comparison in figure 13. The asymptotic profiles (dashed lines) are consistent with the numerical solutions (solid lines) at small x_R. The $\overline{u}_x$ profiles resemble the profiles of the Klebanoff modes appearing in free stream open boundary layers due to free stream vortical disturbances, shown in figure 3 on page 184 of Leib *et al.* (1999). This profile shape is expected because at short distances from the pipe entrance the flow confinement and the base pressure gradient do not play a leading role, a valid representation being given by the free stream boundary-layer region-II profile (3.25). Nevertheless, the amplitude and growth rate of $\overline{u}_x$ in our case are given by $\overline{u}_{\theta,com}$
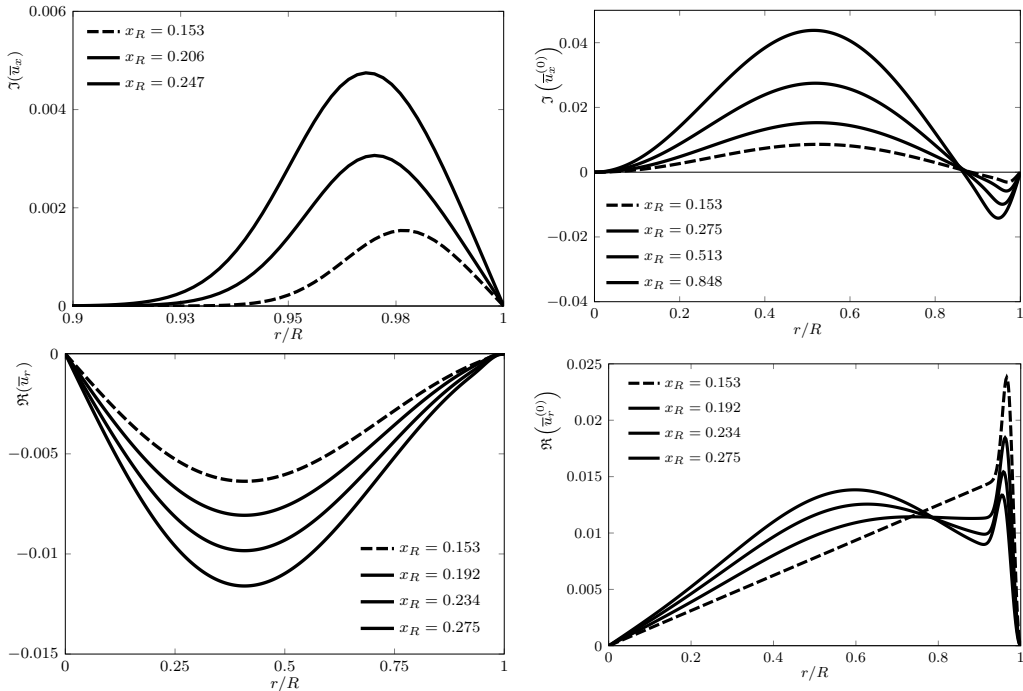
Figure 13: Streamwise and radial velocity components for the Reynolds number and the frequency of Table 2 and $n = 3$, $m = 2$. The solid lines indicate the numerical solutions of the boundary-region equations (2.11) and (2.12) and the dashed lines indicate the asymptotic composite solutions used as initial conditions of the numerical calculations: (3.25) for $\overline{u}_x$, (3.27) for $\overline{u}_x^{(0)}$, (3.26) for $\overline{u}_r$, and (3.32) for $\overline{u}_r^{(0)}$.

in (3.23) and are thus influenced by the presence of the pipe wall. At these locations the dominant part of the total streamwise disturbance velocity $\overline{u}_{x,0}$ is due to $\overline{u}_x^{(0)}$, which is given in (3.27) and is caused by the direct free stream forcing action of the inviscid streamwise velocity in (3.19). The part due to $\overline{u}_x$ is smaller, which means that the streaks have not formed yet and do not dominate the boundary layers over the pipe wall.

4.2.2. *Downstream evolution of the reference-case flow*

The downstream evolution of the disturbance field for the reference case of Table 2 is investigated ($n = 3, m = 4$), assigned as perturbations at the pipe entrance. The inflow perturbations are streamwise-stretched vortices with comparable radial and azimuthal length scales in cross-sectional $r - \theta$ planes and a much longer streamwise wavelength. As discussed in §2.3, at this bulk Reynolds number, $Re_R = 1500$, no TS waves exist, but nevertheless an intense transient growth is detected. This growth is monitored by the energy of the perturbation, defined as

$$\mathcal{E}(x_R) = \pi \underbrace{\int_0^1 |\overline{u}_{x,0}|^2 r_R \mathrm{d}r_R}_{\mathcal{E}_x} + \pi \underbrace{\int_0^1 |\overline{u}_{r,0}|^2 r_R \mathrm{d}r_R}_{\mathcal{E}_r} + \pi \underbrace{\int_0^1 |\overline{u}_{\theta,0}|^2 r_R \mathrm{d}r_R}_{\mathcal{E}_\theta}, \qquad (4.5)$$

where $\overline{u}_{x,0}, \overline{u}_{r,0}, \overline{u}_{\theta,0}$ are defined in (2.7). Figure 14 (left) shows that, while at the entrance the three velocity components have comparable intensity, the streamwise velocity component is the major contributor to the perturbation dynamics as the total energy increases from the pipe inlet, while the other two velocity components decay at comparable rate, as
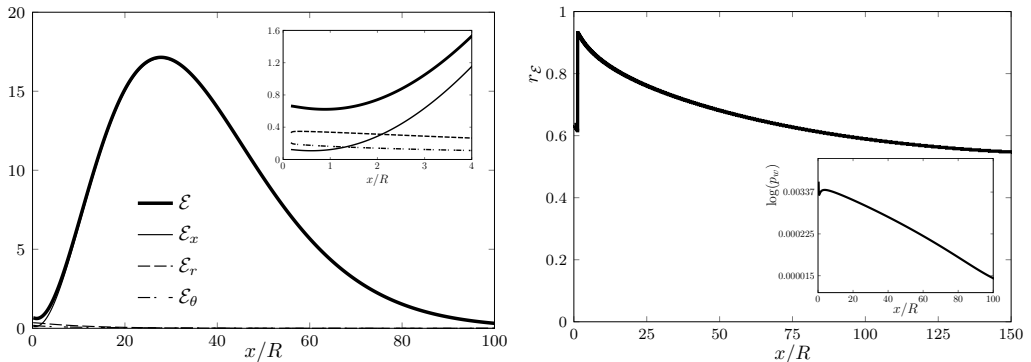
Figure 14: (a) Streamwise evolution of the perturbation energy $\mathcal{E}$ and of its three parts $\mathcal{E}_x, \mathcal{E}_r, \mathcal{E}_\theta$ related to the velocity components. (b) Radial location of the maximum of $\mathcal{E}$ and amplitude of the wall perturbation pressure p_w (inset).

shown in the inset of figure 14 (left). Downstream of $x_R = 20$, the total energy is almost entirely due to $\overline{u}_{x,0}$. It reaches its peak at $x_R = 28$ and then decays monotonically because of viscous dissipation. Almost no perturbation energy is computed downstream of $x_R = 120$. The transient growth is confined to region V, upstream of the fully developed region VI, because the entry region, estimated through the centreline base velocity, terminates at $x_R = 339$. The energy growth and decay is qualitatively similar the transient results in fully developed pipe flows by Reshotko & Tumin (2001) in the spatial case and by O'Sullivan & Breuer (1994) and Trefethen *et al.* (1999) in the temporal case if the time scale is converted to the axial coordinate by use of the streamwise velocity at the pipe axis for qualitative comparison.

As shown in figure 14 (right), the maximum of the perturbation energy near the pipe mouth is confined near the pipe wall, within the base-flow viscous layer. As the flow evolves downstream, the perturbation spreads towards the core of the pipe, although its peak remains in the outer quarter radial region during the entire flow evolution (radial location $r_\mathcal{E} > 0.6$). The inset of figure 14 (right) depicts the downstream evolution of the magnitude of the pressure at the wall, i.e.

$$ p_w(x_R) = |\overline{p}_0(r_R = 1)| = \frac{\lambda_R^3}{4\pi^2} \left| \frac{\partial \overline{u}_{\theta,0}}{\partial r_R} + \frac{\partial^2 \overline{u}_{\theta,0}}{\partial r_R^2} \right|_{r_R=1}. \qquad (4.6) $$

Relation (4.6) is obtained from the θ-momentum equation (S2.8). The wall pressure decays up to $x_R = 0.5$, grows to a maximum at $x_R = 4$, and then decays monotonically downstream.

The radial profiles of $|\overline{u}_{x,0}|$ are shown in figure 15(a), for growing disturbances, and in figure 15(b), for decaying disturbances. The base-flow streamwise gradients enhance the perturbation near the wall and the maximum of $|\overline{u}_{x,0}|$ moves towards the centreline at all streamwise locations. During the growth phase, the wall-shear stress induced by the perturbation remains constant, while it decays when the perturbation energy decreases.

The azimuthal velocity $|\overline{u}_{\theta,0}|$ in figure 16 (left) decays at a faster rate near the centreline and so does the radial velocity $|\overline{u}_{r,0}|$ (not shown). Figure 16 (right) confirms that the pressure $|\overline{p}_0|$ is closely related to $|\overline{u}_{\theta,0}|$ as the near-wall maximum of $|\overline{u}_{\theta,0}|$ is located at the same radial position of the local maximum of $|\overline{p}_0|$, although the overall maximum pressure disturbance is found at the pipe wall.

Figure 17 shows contour plots of the velocity components and pressure at a fixed time instant in a cross-plane where the total perturbation energy reaches its maximum. The
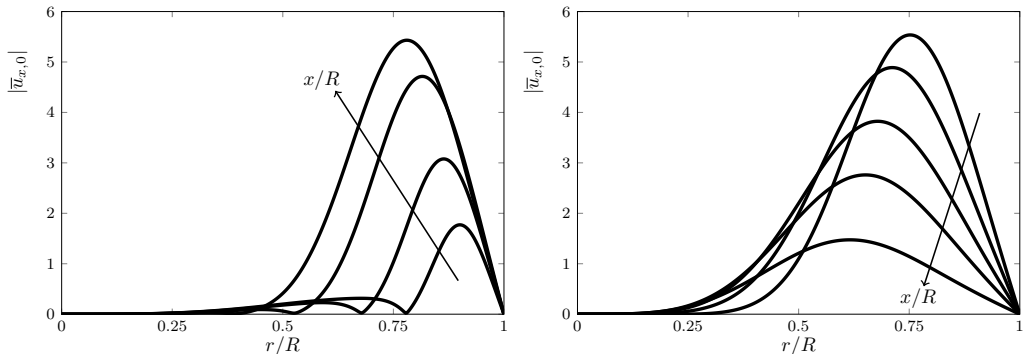
Figure 15: Profiles of the streamwise velocity amplitude $|\overline{u}_{x,0}|$ at different streamwise locations: (a) growing disturbance at $x_R = 3.5, 6.9, 13.7, 20.5$; (b) decaying disturbances at $x_R = 39.2, 51, 62.9, 81.6$.
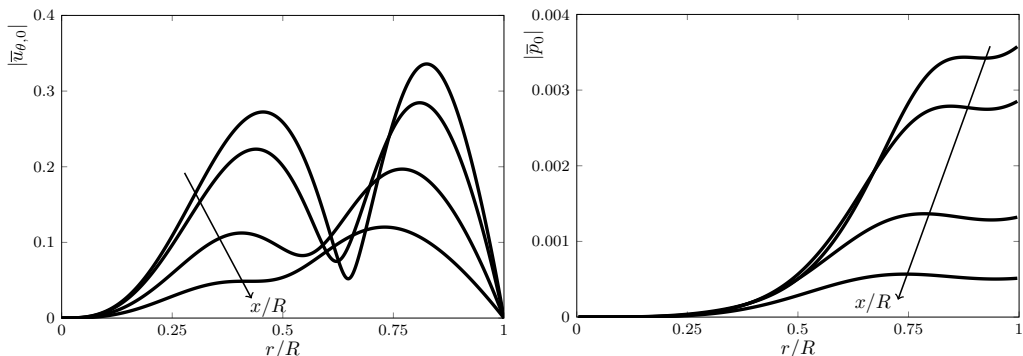

Figure 16: Profiles of the azimuthal velocity amplitude $|\overline{u}_{\theta,0}|$ (a) and of the pressure amplitude $|\overline{p}_0|$ (b) at $x_R = 8.7, 13.7, 28.9, 45.9$.

spanwise and streamwise velocity components appear twisted about the pipe axis with respect to the initial symmetrical distribution observed near the pipe mount, shown in figure 8.

4.2.3. *Effect of Reynolds number*

Figure 18 shows the evolution of the total energy $\mathcal{E}$ at different bulk Reynolds numbers Re_R. As Re_R increases up to approximately $Re_R = 6000$, the perturbation energy increases, with the peak occurring farther downstream. The initial growth rate is independent of Re_R. For $6000 < Re_R < 10000$, the evolution of the energy up to the maximum is Reynolds number independent, while downstream of the peak the energy decays at a slower rate as Re_R increases. This dependence on the Reynolds number also occurs in free stream boundary layers exposed to convected gusts, where the spanwise wavenumber $\kappa = k_z/\mathcal{F}^{1/2}$ is the governing parameter (Leib *et al.* 1999). In figures 5 and 6 of Leib *et al.* (1999), as κ decreases from 1 to 0.1 the the global perturbation energy, dominated by the streamwise velocity, increases and its maximum occurs farther downstream. This behaviour is thus consistent with figure 18, where $\kappa = m/(k_{x,R}Re_R)^{1/2}$ is in the range $0.12 < \kappa < 0.3$ for $1500 < Re_R < 10000$. The radial locations of the energy maxima move closer to the wall at larger Re_R as the boundary layers becomes thinner (not shown).
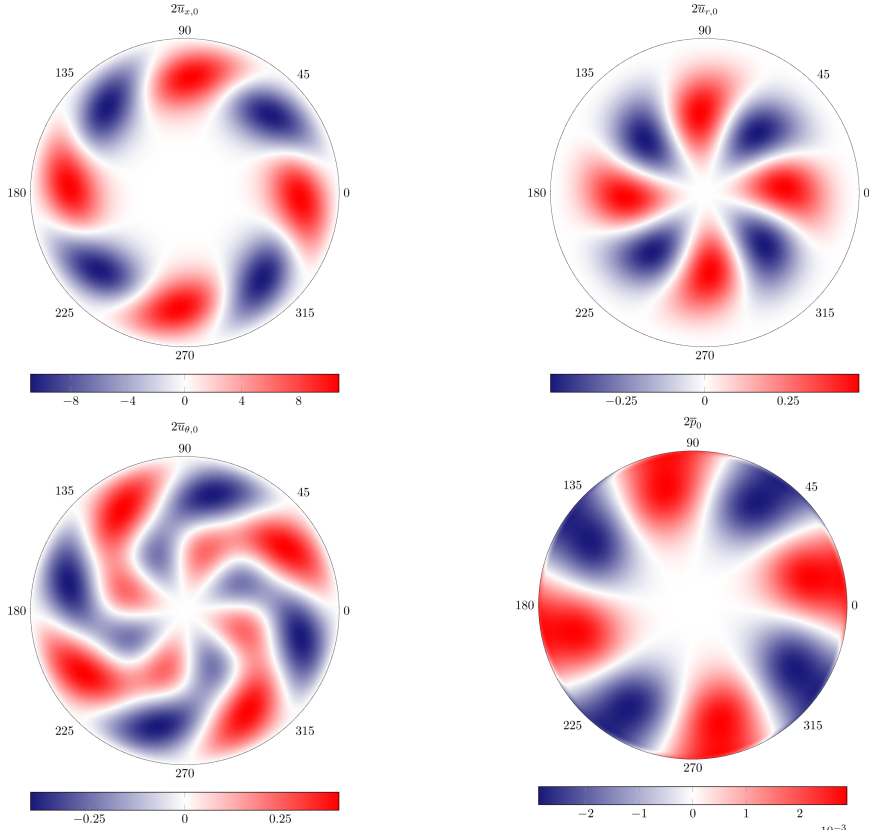
Figure 17: Contours of the instantaneous velocity components $2\overline{u}_{x,0}$, $2\overline{u}_{r,0}$ and $2\overline{u}_{\theta,0}$, and the pressure $2\overline{p}_0$ at $t = 0$, $x_R = 28$, for $Re_R = 1500$, $k_x = 0.118$, $n = 3, m = 4$.
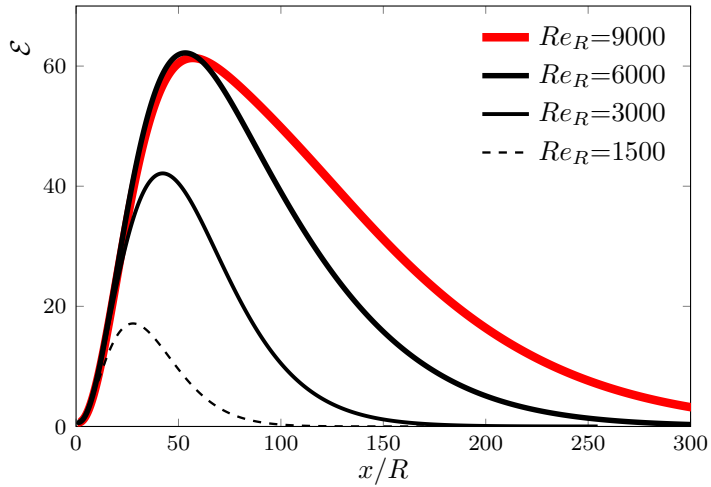

Figure 18: Effect of Re_R on the downstream evolution of perturbation energy $\mathcal{E}$. The dashed line in this figure and in figures 19, 20 and 21 indicates the case of Table 2 ($n = 3, m = 4$).
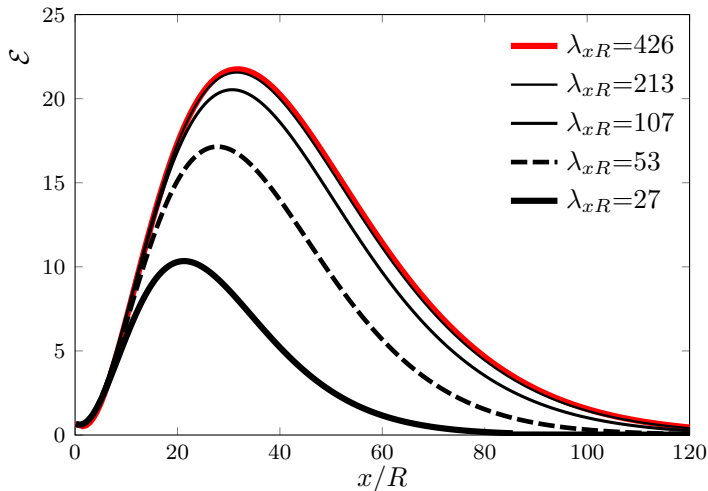
Figure 19: Effect of λ_{xR} on the downstream evolution of total energy $\mathcal{E}$.

4.2.4. *Effect of streamwise wavelength*

Studying the influence of the streamwise wavelength λ_{xR} of the oncoming disturbance is equivalent to studying that of the frequency because the two quantities are inversely proportional to each other and related through U_∞^* for small-amplitude free stream gusts. Figure 19 shows that the initial amplitude of the perturbation energy is independent of λ_{xR}. Up to $x_R = 10$, λ_{xR} has no influence on the disturbance growth as the profiles overlap on one another. Farther downstream, longer wavelengths (i.e. smaller frequencies) lead to perturbations that grow more intensely, with their maxima occurring at larger x_R locations.

The trends at the two highest λ_{xR} overlap (red line and thin black line), showing the independence of the dynamics in the limit of low frequency. The asymptotic scaling at large λ_{xR} can be studied for $\epsilon = \mathcal{F} \ll 1$. In this limit, we introduce $\widehat{U} = U$, $\widehat{V} = \epsilon V$, $\widehat{x} = \overline{x}/\epsilon$ and $\widehat{u}_x = \overline{u}_x/\epsilon$. All the terms in the base-flow equations (2.8)-(2.9) are retained and the coefficient in front of the parenthesis in (2.9) changes to unity. The boundary-region equations (2.11)-(2.12) simplify as all the terms in (2.13)-(2.26) that are proportional to i, which are due to the unsteadiness of the oncoming disturbance (2.1), are asymptotically smaller, and $\mathcal{F}$ changes to unity. The low-frequency disturbance dynamics is thus steady at leading order. The analogous scaling for open free stream boundary layers was first found by Leib *et al.* (1999) on pages 183–185. In figure 19, the behaviour is consistent with the asymptotic analysis for $\epsilon \ll 1$: Re_R is constant for those cases and thus it does not affect the scaling $\widehat{x}$. At leading order the total energy is

$$\mathcal{E} \sim \frac{\pi m^2}{k_x^2} \int_0^1 |\widehat{u}_x|^2 r_R \mathrm{d}r_R = 4\pi^3 Re_R^2 \int_0^1 |\widehat{u}_x|^2 r_R \mathrm{d}r_R, \qquad (4.7)$$

which is independent of λ_{xR}. The prediction that the optimum conditions leading to the maximum transient growth are steady is fully consistent with the optimal-growth results of vortical perturbations that are present inside a Blasius boundary layer and evolve downstream from locations near the leading edge (Andersson *et al.* 1999; Luchini 2000). Figure 19 shows that oncoming perturbations with measurable unsteadiness, i.e. with frequency $f^* = 1$Hz ($\lambda_{xR} = 200$) for the air pipe in Table 2, are equally likely to lead to the flow breakdown as they achieve a growth which is very close to the optimal one.
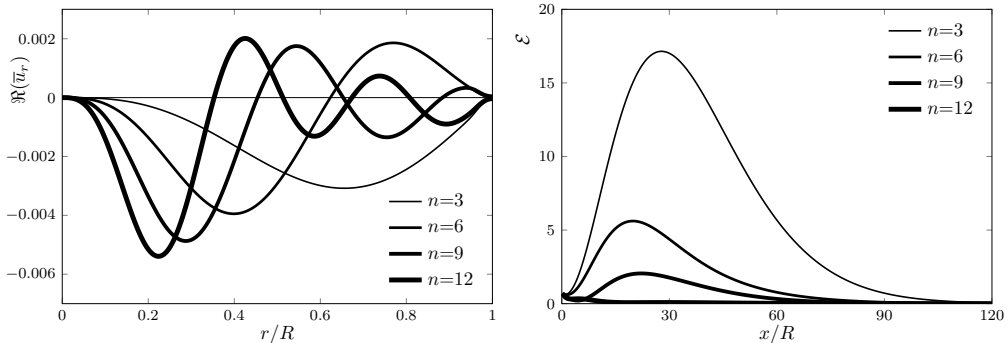
Figure 20: (a) Real part of $\overline{u}_r$ for $m = 4$ at $x_R = 0.18$. (b) Effect of n on the downstream evolution of total energy $\mathcal{E}$ for $m = 4$.

4.2.5. *Effect of radial characteristic scale*

In the expansion based on Fourier–Bessel coefficients (2.1), the characteristic radial scale is defined by the zeros of the Bessel function ξ_{mn}. For fixed azimuthal index m, the larger the radial coefficient n, the smaller the radial length scale, as shown in figure 20 (left) by the profiles of the real part of $\overline{u}_r$ at small x_R locations. The transient growth decreases as the radial length scale of the free stream disturbance becomes smaller, as shown in figure 20 (right). This effect is due to the more intense viscous dissipation caused by the large velocity gradients related to the small radial scale. The location of the maximum energy is computed closer to the pipe inlet as the radial scale decreases. For a Fourier-Bessel coefficient $n = 9$, the perturbation decreases upstream of the expected transient growth and subsequent viscous dissipation. For $n = 12$, the perturbation decreases at any streamwise location.

The influence of the radial scale on the disturbance evolution cannot be investigated through the non-normality of the eigenfunctions of the developing boundary layers on the pipe wall. An eigenvalue-based approach would model the near-entrance disturbance as completely confined within the base-flow boundary layer, whereas the radial scale only pertains to the free stream gust flow and does not enter the classical stability problem of the boundary layer. The adopted boundary-region approach instead takes into account all the characteristics of the gust flow because, being an initial-value problem, the specification of the pipe-entrance flow is vital for the evolution of the perturbation inside the pipe.

4.2.6. *Effect of azimuthal wavelength*

Figure 21 (left) shows the real part of $\overline{u}_\theta$ for $n = 6$ near the pipe mouth, at $x_R = 0.18$, for different $\lambda_{zR} = 2\pi/m$. For this n value, varying m only impacts on the azimuthal modulation of the disturbance, while the characteristic radial scale is maintained. The influence of the azimuthal wavelength λ_{zR} on the perturbation energy inside the pipe is shown in figure 21 (right). There exists an optimal λ_{zR} (the reference $\lambda_{zR} = 2.09$, $m = 3$) that leads to the most energetic growth. This azimuthal coefficient was also found to lead to the most energetic spatial transient disturbance by Mayer & Reshotko (1997) in a fully developed laminar flow. Disturbances with smaller λ_{zR} are influenced by viscous dissipation that hampers their growth. Oncoming disturbances with a larger azimuthal wavelength, $\lambda_{zR} = 3.14$ ($m = 2$) are almost two-dimensional and do not lead to the maximum growth because the dynamics of the streaks is a strictly three-dimensional phenomenon (Leib *et al.* 1999), unlike TS waves, the amplification of which is maximum in the two-dimensional case (Schmid & Henningson 2001). The perturbations
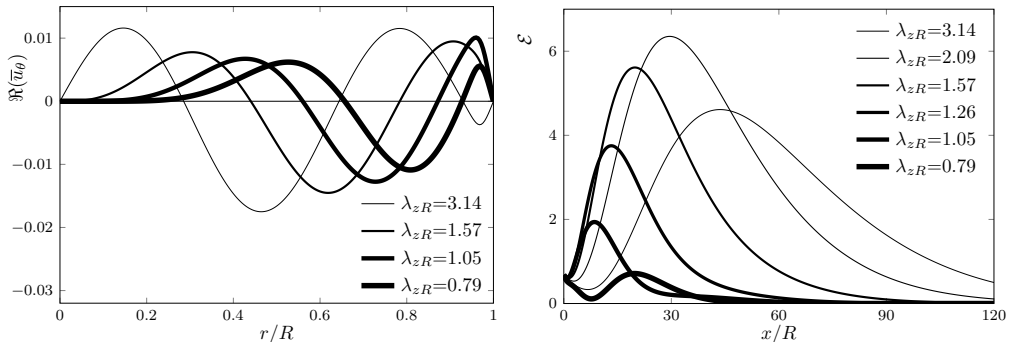
Figure 21: (a) Real part of $\overline{w}$ for $n = 6$ at $x_R = 0.18$. (b) Effect of λ_{zR} on the downstream evolution of total energy $\mathcal{E}$.

with $\lambda_{zR} = 3.14$ persist downstream to larger distances than in the optimal case because they are less influenced by viscous dissipation due to azimuthal shear effects.

4.2.7. *Comparison with experimental and numerical data*

Wygnanski & Champagne (1973) experimentally studied the air flow in the entrance region of a circular pipe in order to understand the formation of turbulent slug and puffs. Just like Reynolds (1883), they recognized the impact of the entry disturbances on the flow character farther downstream, especially the intensity of inlet perturbations. They utilized an orifice, a suspended circular disk and a honeycomb to generate the perturbation at the pipe mouth. In the entrance region, i.e. where the flow is stable according to classical stability theory, Wygnanski & Champagne (1973) detected intense growth of low-frequency oscillations upstream of the turbulent region and proposed that '...the growth of perturbations is associated with the large shear existing within the boundary layer...'. They also observed that the longitudinal fluctuations rose abruptly, much more than the cross-flow velocity components. These experimental results fully agree with our theoretical results.

Figure 22 shows their flow visualization of the pipe entrance flow by dye injection at two downstream locations. It is evident that, upstream of where the flow breaks down to turbulent puffs (right-hand part of figure 22a), the disturbances are elongated in the axial direction and characterized by a well-defined azimuthal length scale, as predicted by the low-frequency theory.

Figure 23 presents a comparison between our calculations and three sets of experimental data by Wygnanski & Champagne (1973). In figure 23(a,b), the base-flow comparison is excellent for the case at low level of free stream turbulence (figure 23a, $|u'|/\overline{U}_{cl} = 0.16\%$, where $\overline{U}_{cl}$ is the centreline mean velocity), whereas the experimental base-flow data at much higher levels of free stream turbulence (top right graph, $|u'|/\overline{U}_{cl} = 5.8\%$, and 7.8%) deviate considerably from the base flow computed via (2.8) and (2.9). These results are expected because, when the oncoming disturbances are weak (generated by the upstream honeycomb), the nonlinear effects on the perturbation dynamics are negligible and do not distort the laminar base flow. When the disturbances are more intense (generated by the orifice and the suspended disk), nonlinearity distorts the base flow, even though the flow has not broken down to turbulence. The comparisons of the perturbation data, shown in figure 23(c,d), are consistent with the mean-flow results, i.e. much better agreement is obtained in the left graph, where nonlinear effects are likely to play a marginal role. The results in figure 23(c) are robust because the profile shape varies only slightly when the frequency, and the azimuthal and radial indexes, m and n, are varied independently
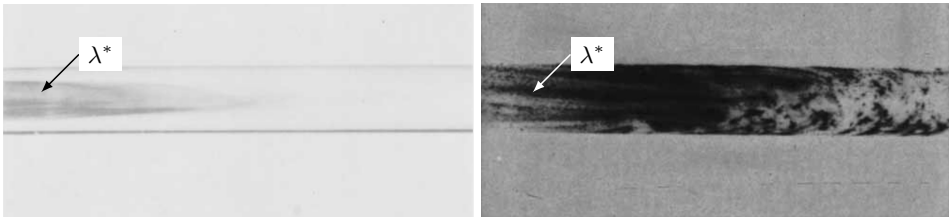
Figure 22: Visualization of flow disturbances at $x_R = 60$ (left) and $x_R = 100$ (right) for an air flow in a pipe at $Re_R = 1250$ (Wygnanski & Champagne 1973). The arrows indicate the azimuthal wavelength in the developing regions. The flows are from the left to the right.

about the reference case $k_{x,R} = 0.118$, $n = 2$, $m = 3$. The flow parameter ranges were chosen based on the description of the experimental conditions given in Wygnanski & Champagne (1973), i.e. streamwise wavelength longer than the radius and comparable azimuthal and radial length scales because generated by the honeycomb upstream of the pipe entrance. It would certainly be interesting to carry out further comparisons between better controlled experiments and computations of the nonlinear boundary-region equations and direct numerical simulations.

Wu *et al.* (2015) studied the pipe-flow entrance problem via direct numerical simulations. In one of their cases at $Re_R = 4000$, the flow at the pipe inlet was a superposition of a uniform base flow and vortical disturbances located near the pipe wall with a quite distinct azimuthal modulation. The perturbation did not grow as the base flow evolved along the entry region and the breakdown to turbulence was detected much farther downstream, i.e. at locations where the laminar base flow reached the parabolic profile. This result qualitatively agrees with our theoretical prediction. A visual inspection of their figure 1D leads to an estimate of $m = 8$ or larger, that is, sufficient for viscous effects to dominate and attenuate the algebraic growth, as observed in figure 21 ($m = 8$ corresponds to $\lambda_{zR} = 0.79$).

5. Conclusions

In this paper, we have presented the first theoretical study of the entrainment and growth of unsteady three-dimensional vortical disturbances in the entrance region of an incompressible pipe flow, as a step towards the full comprehension of laminar to turbulent transition in confined flows. This fundamental problem has been central in the fluid mechanics research community since the pioneering work of Reynolds (1883). In the other theoretical studies of the pipe-entrance flow, the entrainment of disturbances in the confined space was not studied because velocity or pressure fluctuations were absent in the pipe core flow and were only present in the viscous boundary layer attached to the pipe wall (references in §1.3).

The mathematical framework takes inspiration from the pioneering work by Leib *et al.* (1999) on the generation of low-speed streaks in a flat-plate boundary layer. The analysis is based on the method of matched asymptotic expansions and on the assumptions of high Reynolds number and of flow perturbations of low amplitude and frequency. The low-frequency hypothesis has been motivated by the evidence that these disturbances amplify the most in free stream boundary layers to form streamwise-elongated streaks. This approach has allowed for an analytical description of realistic vortical perturbations that can be created in a laboratory set-up at the pipe inlet. The effects of the pipe confinement, the streamwise pressure gradient, the viscous/inviscid interplay and the interactions
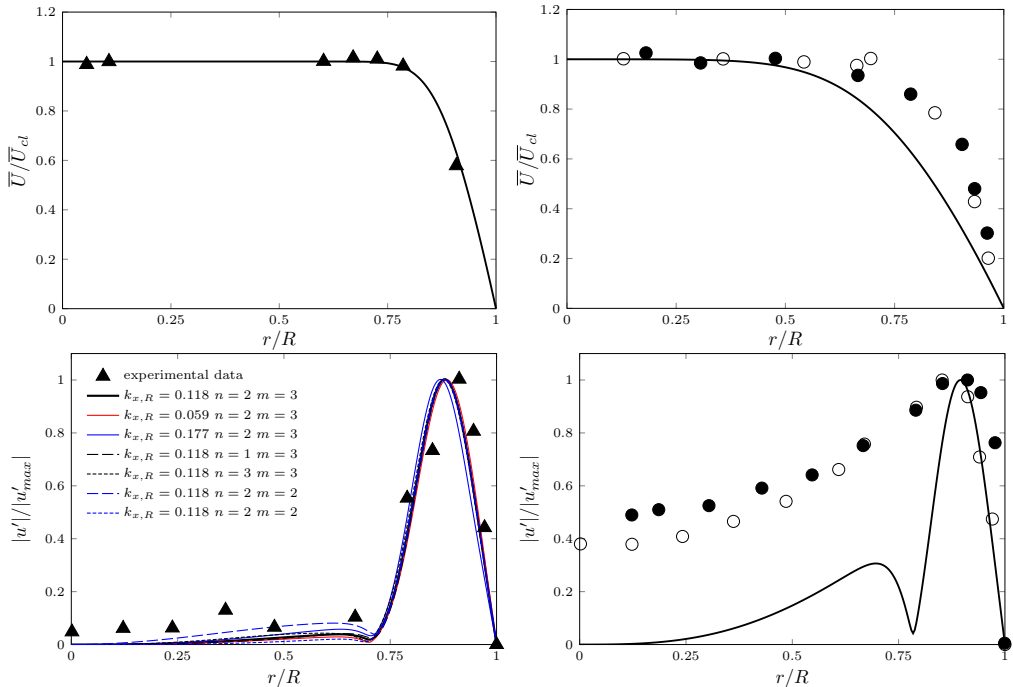
Figure 23: Experimental data by Wygnanski & Champagne (1973) (symbols) and numerical profiles (solid lines) at $x_R = 30$. Top: base-flow streamwise velocity, computed by solving (2.8) and (2.9); bottom: perturbation-flow streamwise velocity $\epsilon|\overline{u}_{x,0}|$ normalized by the maximum value, computed by solving (2.11) and (2.12). Left: $Re_R = 9500$ and $|u'|/\overline{U}_{cl} = 0.16\%$; right: $Re_R = 1200$ and $|u'|/\overline{U}_{cl} = 5.8\%$ (white circles) and $|u'|/\overline{U}_{cl} = 7.8\%$ (black circles). Here $\overline{U}_{cl}$ denotes the centreline base-flow velocity. For all cases, the reference flow parameters are $k_{x,R} = 0.118$, $n = 2$, $m = 3$.

amongst the velocity components have been revealed. The amplitude of the initial disturbance is related uniquely to that of the oncoming free stream perturbation. The composite velocity profiles of the disturbance flow have been useful for the specification of the appropriate initial conditions for the boundary-region perturbation equations.

The base-flow velocity components and pressure gradient agree with results from direct numerical simulations and experiments. We propose to utilize the second derivative of the base flow at the pipe centreline to ascertain whether the flow has reached the fully developed Poiseuille flow. This method is the most conservative one among those tested for quantifying the entry length because the pipe axis is the last location where the base flow is subject to the diffusing viscous effects. Near the pipe mouth, the base pressure gradient plays a minimal role and the disturbance flow is mostly dominant within the boundary layer at the pipe wall. The perturbations appear in the form of streamwise-elongated streaky structures and eventually evolve towards the pipe core, where the base flow is still mostly inviscid. The disturbance growth is enhanced as the frequency decreases, and the bulk Reynolds number and the characteristic radial length scale increase. The azimuthal wavelength that generates the most intense downstream growth has also been computed.

The significant algebraic growth and the viscous decay only occur in the entrance region, i.e. where the base flow is still streamwise dependent. Nevertheless, as evident from the direct numerical simulations of Wu *et al.* (2015), vortical disturbances that

initially decay from the pipe inlet may trigger nonlinear effect farther downstream and lead the flow to the breakdown to turbulence. Our results compare favourably with the experimental data of Wygnanski & Champagne (1973) when the amplitude of the oncoming perturbation is low, thus suggesting that the linearized dynamics is valid. The less satisfactory agreement for more intense perturbations highlights the urgency for the inclusion of the nonlinear effects. We therefore plan to extend our analysis by relaxing the assumption of small amplitude to study the nonlinear dynamics and to explore the link between the perturbations generated at the pipe inlet and the travelling waves discovered by Faisst & Eckhardt (2003) and Wedin & Kerswell (2004). Accurate experimental data are also required in order to further test our results.

Acknowledgements

Declaration of interests

The authors report no conflict of interest.

REFERENCES

ALIZARD, F., CADIOU, A., LE PENVEN, L., DI PIERRO, B. & BUFFAT, M. 2018 Space-time dynamics of optimal wavepackets for streaks in a channel entrance flow. *J. Fluid Mech.* **844**, 669–706.

ANDERSSON, P., BERGGREN, M. & HENNINGSON, D.S. 1999 Optimal disturbances and bypass transition in boundary layers. *Phys. Fluids* **11** (1), 134–150.

AVILA, K., MOXEY, D., DE LOZAR, A., AVILA, M., BARKLEY, D. & HOF, B. 2011 The onset of turbulence in pipe flow. *Science* **333** (6039), 192–196.

AVILA, M., MELLIBOVSKY, F., ROLAND, N. & HOF, B. 2013 Streamwise-localized solutions at the onset of turbulence in pipe flow. *Phys. Rev. Lett.* **110** (22), 224502.

AVILA, M., WILLIS, A.P. & HOF, B. 2010 On the transient nature of localized pipe flow turbulence. *J. Fluid Mech.* **646**, 127–136.

BERGSTRÖM, L. 1993 Optimal growth of small disturbances in pipe Poiseuille flow. *Phys. Fluids* **5** (11), 2710–2720.

BORODULIN, V.I., IVANOV, A.V., KACHANOV, Y.S. & ROSCHEKTAYEV, A.P. 2021*a* Distributed vortex receptivity of a swept-wing boundary layer. Part 1. Efficient excitation of CF modes. *J. Fluid Mech.* **908** (A14).

BORODULIN, V.I., IVANOV, A.V., KACHANOV, Y.S. & ROSCHEKTAYEV, A.P. 2021*b* Distributed vortex receptivity of a swept-wing boundary layer. Part 2. Receptivity characteristics. *J. Fluid Mech.* **908** (A15).

BRANDT, L., SCHLATTER, P. & HENNINGSON, D.S. 2004 Transition in boundary layers subject to free-stream turbulence. *J. Fluid Mech.* **517**, 167–198.

BUFFAT, M., LE PENVEN, L., CADIOU, A. & MONTAGNIER, J. 2014 DNS of bypass transition in entrance channel flow induced by boundary layer interaction. *Eur. J. Mech. - B/Fluids* **43**, 1–13.

CORCOS, G.M. & SELLARS, J.R. 1959 On the stability of fully developed flow in a pipe. *J. Fluid Mech* **5** (1), 97–112.

CROWDER, H.J. & DALTON, C. 1971 On the stability of Poiseuille flow in a pipe. *J. Comp. Phys.* **7** (1), 12–31.

DAVEY, A. 1978 On Itoh's finite amplitude stability theory for pipe flow. *J. Fluid Mech.* **86** (4), 695–703.

DAVEY, A. & NGUYEN, H.P.F. 1971 Finite-amplitude stability of pipe flow. *J. Fluid Mech.* **45** (4), 701–720.

DETTMAN, J.W. 1965 *Applied complex variables*. Courier Corporation.

DIETZ, A.J. 1999 Local boundary-layer receptivity to a convected free-stream disturbance. *J. Fluid Mech.* **378**, 291–317.

DRAAD, A.A., KUIKEN, G.D.C. & NIEUWSTADT, F.T.M. 1998 Laminar-turbulent transition in pipe flow for Newtonian and non-Newtonian fluids. *J. Fluid Mech.* **377**, 267–312.

DRAZIN, P.G. & REID, W.H. 2004 *Hydrodynamic stability*. Cambridge Mathematical Library.

DUCK, P.W. 2005 Transient growth in developing plane and Hagen Poiseuille flow. *Proc. Royal Soc. London. Series A.* **461**, 1311–1333.

DUCK, P.W. 2006 Nonlinear growth (and breakdown) of disturbances in developing Hagen Poiseuille flow. *Phys. Fluids* **18** (6), 064103.

DUGUET, Y., WILLIS, A.P. & KERSWELL, R.R. 2008 Transition in pipe flow: the saddle structure on the boundary of turbulence. *J. Fluid Mech.* **613**, 255–274.

DURST, F., RAY, S., ÜNSAL, B. & BAYOUMI, O.A. 2005 The development lengths of laminar pipe and channel flows. *J. Fluids Eng.* **127** (6), 1154–1160.

ECKHARDT, B. 2007 Turbulence transition in pipe flow: some open questions. *Nonlinearity* **21** (1), T1.

ECKHARDT, B. 2009 Introduction. Turbulence transition in pipe flow: 125th anniversary of the publication of Reynolds' paper. *Phil. Trans. R. Soc. A* **367**, 449–455.

ECKHARDT, B., SCHNEIDER, T.M., HOF, B. & WESTERWEEL, J. 2007 Turbulence transition in pipe flow. *Annu. Rev. Fluid Mech.* **39**, 447–468.

FAISST, H. & ECKHARDT, B. 2003 Traveling waves in pipe flow. *Phys. Rev. Lett.* **91** (**22**) (224502).

FOX, J.A., LESSEN, M. & BHAT, W.V. 1968 Experimental investigation of the stability of Hagen-Poiseuille flow. *Phys. Fluids* **11** (1), 1–4.

GARG, V.K. 1981 Stability of developing flow in a pipe: non-axisymmetric disturbances. *J. Fluid Mech.* **110**, 209–216.

GILL, A.E. 1965 On the behaviour of small disturbances to Poiseuille flow in a circular pipe. *J. Fluid Mech.* **21** (1), 145–172.

GOLDSTEIN, M.E. 1978 Unsteady vortical and entropic distortions of potential flows round arbitrary obstacles. *J. Fluid Mech.* **89**, 433–468.

GUPTA, S.C. & GARG, V.K. 1981 Effect of velocity distribution on the stability of developing flow in a pipe. *Phys. Fluids* **24** (4), 576–578.

HOF, B., DE LOZAR, A., KUIK, D.J. & WESTERWEEL, J. 2008 Repeller or attractor? Selecting the dynamical model for the onset of turbulence in pipe flow. *Phys. Rev. Lett.* **101** (21), 214501.

HOF, B., VAN DOORNE, C.W.H., WESTERWEEL, J. & NIEUWSTADT, F.T.M. 2005 Turbulence regeneration in pipe flow at moderate Reynolds numbers. *Phys. Rev. Lett.* **95** (21), 214502.

HOF, B., VAN DOORNE, C.W.H., WESTERWEEL, J., NIEUWSTADT, F.T.M., FAISST, H., ECKHARDT, B., WEDIN, H., KERSWELL, R.R. & WALEFFE, F. 2004 Experimental observation of nonlinear traveling waves in turbulent pipe flow. *Science* **305** (5690), 1594–1598.

HORNBECK, R.W. 1964 Laminar flow in the entrance region of a pipe. *Appl. Sci. Res.* **13**, 224–232.

HUANG, L.M. & CHEN, T.S. 1974a Stability of developing pipe flow subjected to non-axisymetric disturbances. *J. Fluid Mech.* **63** (Part 1), 183–193.

HUANG, L.M. & CHEN, T.S. 1974b Stability of the developing laminar pipe flow. *Phys. Fluids* **17**, 245–247.

ITOH, N. 1977 Nonlinear stability of parallel flows with subcritical Reynolds numbers. Part 2. Stability of pipe Poiseuille flow to finite axisymmetric disturbances. *J. Fluid Mech.* **82** (3), 469–479.

JACOBS, R.G. & DURBIN, P.A. 2001 Simulation of bypass transition. *J. Fluid Mech.* **428**, 185–212.

KASKEL, A. 1961 Experimental study of the stability of pipe flow. II. Development of disturbance generator. *Jet Propulsion Lab. Tech. Rep* pp. 32–138.

Kerswell, R.R. 2005 Recent progress in understanding the transition to turbulence in a pipe. *Nonlinearity* **18** (6), R17.

Kim, J., Moin, P. & Moser, R. 1987 Turbulence statistics in fully developed channel flow at low Reynolds number. *J. Fluid Mech.* **177**, 133–166.

Leib, S.J., Wundrow, D.W. & Goldstein, M.E. 1999 Effect of free-stream turbulence and other vortical disturbances on a laminar boundary layer. *J. Fluid Mech.* **380**, 169–203.

Lessen, M., Sadler, G.S. & Liu, T.Y. 1968 Stability of pipe Poiseuille flow. *Phys. Fluids* **11**, 1404–1409.

Luchini, P. 1996 Reynolds-number-independent instability of the boundary layer over a flat surface. *J. Fluid Mech.* **327**, 101–115.

Luchini, P. 2000 Reynolds-number-independent instability of the boundary layer over a flat surface: optimal perturbations. *J. Fluid Mech.* **404**, 289–309.

Marensi, E., Ricco, P. & Wu, X. 2017 Nonlinear unsteady streaks engendered by the interaction of free-stream vorticity with a compressible boundary layer. *J. Fluid Mech.* **817**, 80–121.

Matsubara, M. & Alfredsson, P.H. 2001 Disturbance growth in boundary layers subjected to free-stream turbulence. *J. Fluid Mech.* **430**, 149–168.

Mayer, E.W. & Reshotko, E. 1997 Evidence for transient disturbance growth in a 1961 pipe-flow experiment. *Phys. Fluids* **9** (1), 242–244.

Meseguer, A. 2003 Streak breakdown instability in pipe Poiseuille flow. *Phys. Fluids* **15** (5), 1203–1213.

Mohanty, A.K. & Asthana, S.B.L. 1978 Laminar flow in the entrance region of a smooth pipe. *J. Fluid Mech.* **90**, 433–447.

Mullin, T. 2011 Experimental studies of transition to turbulence in a pipe. *Ann. Rev. Fluid Mech.* **43**, 1–24.

O'Sullivan, P.L. & Breuer, K.S. 1994 Transient growth in circular pipe flow. I. Linear disturbances. *Phys. Fluids* **6** (11), 3643–3651.

Panton, R. 2013 *Incompressible Flow*. Wiley-Interscience – Fourth Edition.

Patera, A.T. & Orszag, S.A. 1981 Finite-amplitude stability of axisymmetric pipe flow. *J. Fluid Mech.* **112**, 467–474.

Pedley, T.J. 1969 On the instability of viscous flow in a rapidly rotating pipe. *J. Fluid Mech.* **35** (1), 97–115.

Pekeris, C.L. 1948 Stability of the laminar flow through a straight pipe of circular cross-section to infinitesimal disturbances which are symmetrical about the axis of the pipe. *PNAS* **34** (6), 285.

Rayleigh, L. 1892 On the instability of cylindrical fluid surfaces. *Phil. Mag.* **34** (5), 177–180.

Reshotko, E. 1958 Jet propulsion lab. *Pasadena, California, Rep.* (20-364).

Reshotko, E. & Tumin, A. 2001 Spatial theory of optimal disturbances in a circular pipe flow. *Phys. Fluids* **13** (4), 991–996.

Reynolds, O. 1883 An experimental investigation of the circumstances which determine whether the motion of water shall be direct or sinuous, and of the law of resistance in parallel channels. *Phil. Trans. R. Soc.* **35** (224-226), 84–99.

Ricco, P., Luo, J. & Wu, X. 2011 Evolution and instability of unsteady nonlinear streaks generated by free-stream vortical disturbances. *J. Fluid Mech.* **677**, 1–38.

Rosenhead, L. 1963 *Laminar Boundary Layers*. Dover.

Rubin, S.G., Khosla, P.K. & Saari, S. 1977 Laminar flow in rectangular channels. *Computers and Fluids* **5**, 151–173.

Sahu, K.C. & Govindarajan, R. 2007 Linear instability of entry flow in a pipe. *J. Fluids Eng.* **129** (10), 1277–1280.

Salwen, H., Cotton, F.W. & Grosch, C.E. 1980 Linear stability of Poiseuille flow in a circular pipe. *J. Fluid Mech.* **98**, 273–84.

Sarpkaya, T. 1975 A note on the stability of developing laminar pipe flow subjected to axisymmetric and non-axisymmetric disturbances. *J. Fluid Mech.* **68** (2), 345–351.

Schmid, P.J. & Henningson, D.S. 1994 Optimal energy density growth in Hagen-Poiseuille flow. *J. Fluid Mech.* **277**, 197–225.

Schmid, P.J. & Henningson, D.S. 2001 *Stability and Transition in Shear Flows*. Applied Mathematical Sciences, Springer, Vol. 142).

Sexl, T. 1927 On the stability question of the Poiseuille and Couette currents. *Ann. Phys.* **388** (14), 835–848.

Shapiro, A.H., Siegel, R. & Kline, S.J. 1954 Friction factor in the laminar entry region of a smooth tube. In *J. Appl. Mech. Trans. ASME*, , vol. 21, pp. 289–289.

da Silva, D.F. & Moss, E.A. 1994 The stability of pipe entrance flows subjected to axisymmetric disturbances. *J. Fluid Eng.* **116**, 61–65.

Smith, F.T. & Bodonyi, R.J. 1980 On the stability of the developing flow in a channel or circular pipe. *Quart. J. Mech. Appl. Math.* **33** (3), 293–320.

Smith, F.T. & Bodonyi, R.J. 1982 Amplitude-dependent neutral modes in the Hagen-Poiseuille flow through a circular pipe. *Proc. Royal Soc. London* **384** (1787), 463–489.

Sparrow, E.M., Lin, S.H. & Lundgren, T.S. 1964 Flow development in the hydrodynamic entrance region of tubes and ducts. *Phys. Fluids* **7** (3), 338–347.

Tatsumi, T. 1952 Stability of the laminar inlet-flow prior to the formation of Poiseuille regime, II. *J. Phys. Soc. Japan* **7** (5), 495–502.

Trefethen, A.E., Trefethen, L.N. & Schmid, P.J. 1999 Spectra and pseudospectra for pipe Poiseuille flow. *Computer Meth. Appl. Mech. Eng.* **175** (3-4), 413–420.

Wedin, H. & Kerswell, R.R. 2004 Exact coherent structures in pipe flow: travelling wave solutions. *J. Fluid Mech.* **508**, 333–371.

Wilson, S.D.R. 1970 Entry flow in a channel. Part 2. *J. Fluid Mech.* **46**, 787–799.

Wu, X., Moin, P. & Adrian, R.J. 2020 Laminar to fully turbulent flow in a pipe: scalar patches, structural duality of turbulent spots and transitional overshoot. *J. Fluid Mech.* **896** (A9).

Wu, X., Moin, P., Adrian, R.J. & Baltzer, J.R. 2015 Osborne Reynolds pipe flow: direct simulation from laminar through gradual transition to fully developed turbulence. *PNAS* **112** (26), 7920–7924.

Wygnanski, I.J. & Champagne, F.H. 1973 On transition in a pipe. Part 1. The origin of puffs and slugs and the flow in a turbulent slug. *J. Fluid Mech.* **59**, 281–335.

Zanoun, E.-S., Kito, M. & Egbers, C. 2009 A study on flow transition and development in circular and rectangular ducts. *J. Fluids Eng.* **131** (6), 061204.

Growth of vortical disturbances entrained in the entrance region of a circular pipe - supplementary material

Pierre Ricco[1]† and Claudia Alvarenga[1,2]

[1]Department of Mechanical Engineering, The University of Sheffield, S1 3JD Sheffield, United Kingdom
[2]Department of Fluid Dynamics, A*Star Institute of High Performance Computing, Singapore

This supplementary material presents further analysis that is used in the paper and additional theoretical and numerical results.

S1. Numerical procedures

The base-flow boundary-layer and continuity equations (2.8)-(2.9), supplemented by the mass conservation law, are discretized according to a scheme that is an improved version of that used by Hornbeck (1964). The base-flow streamwise velocity and pressure fields are computed simultaneously and the base-flow radial velocity is computed a posteriori through the continuity equation. A difference from Hornbeck (1964) regards the treatment of the nonlinear convective terms in the base-flow x-momentum equation (2.9). In their paper, these terms are linearized, i.e., the values at the previous x locations are used in the nonlinear terms. Here, we instead use a predictor-corrector method for the computation of the convective terms at step $\overline{n}$. In the predictor step $\overline{n} - 1$, an initial approximation of the streamwise velocity and pressure fields is calculated via the linearized discretized equations as in Hornbeck (1964). In the corrector step, new values of $U^{\overline{n}}$ and $P^{\overline{n}}$ are computed, using $U^{\overline{n}-1}$ and $P^{\overline{n}-1}$ in the discretization of the convective terms instead of those at the previous streamwise location. This procedure is repeated iteratively until convergence is reached. The convergence criterion is based on the radial velocity gradient at the wall, $\partial U/\partial r|_{r=R}$. The asymptotic composite solution derived in §3.1 is used as initial condition at small $\overline{x}$ values.

The perturbation equations (2.11)-(2.12) are discretized using backward and central finite-difference schemes in $\overline{x}$ and r, respectively. The degree of the radial velocity equation (2.11) is reduced from fourth to second by defining the radial second derivative of $\overline{u}_r$ as a new variable. The resulting system is written in the form of a block tridiagonal matrix and solved at each $\overline{x}$ by the Thomas algorithm (Cebeci 2002). The asymptotic composite solution given in §3.2 is used as initial condition at small $\overline{x}$ values. At each $\overline{x}$ location the behaviour of the velocity field as the pipe axis is approached is checked against the asymptotic results of Lewis & Bellan (1990), discussed in §S3.2.

† Email address for correspondence: p.ricco@sheffield.ac.uk

S2. Boundary-region equations

We herein derive the final form of the boundary-region equations. In expanded form, equations (2.3) and (2.4) read

$$\frac{1}{r}\frac{\partial}{\partial r}\left(ru_r\right) + \frac{1}{r}\frac{\partial u_\theta}{\partial \theta} + \frac{\partial u_x}{\partial x} = 0, \tag{S2.1}$$

$$\frac{\partial u_x}{\partial t} + u_x\frac{\partial u_x}{\partial x} + u_r\frac{\partial u_x}{\partial r} + \frac{u_\theta}{r}\frac{\partial u_x}{\partial \theta} = -\frac{\partial p}{\partial x} + \frac{1}{Re_\lambda}\frac{\partial^2 u_x}{\partial x^2} +$$
$$\frac{1}{rRe_\lambda}\frac{\partial}{\partial r}\left(r\frac{\partial u_x}{\partial r}\right) + \frac{1}{r^2 Re_\lambda}\frac{\partial^2 u_x}{\partial \theta^2}, \tag{S2.2}$$

$$\frac{\partial u_r}{\partial t} + u_x\frac{\partial u_r}{\partial x} + u_r\frac{\partial u_r}{\partial r} + \frac{u_\theta}{r}\frac{\partial u_r}{\partial \theta} - \frac{u_\theta^2}{r} = -\frac{\partial p}{\partial r} + \frac{1}{Re_\lambda}\frac{\partial^2 u_r}{\partial x^2} +$$
$$\frac{1}{Re_\lambda}\frac{\partial}{\partial r}\left[\frac{1}{r}\frac{\partial(ru_r)}{\partial r}\right] + \frac{1}{r^2 Re_\lambda}\frac{\partial^2 u_r}{\partial \theta^2} - \frac{2}{r^2 Re_\lambda}\frac{\partial u_\theta}{\partial \theta}, \tag{S2.3}$$

$$\frac{\partial u_\theta}{\partial t} + u_x\frac{\partial u_\theta}{\partial x} + u_r\frac{\partial u_\theta}{\partial r} + \frac{u_\theta}{r}\frac{\partial u_\theta}{\partial \theta} + \frac{u_r u_\theta}{r} = -\frac{1}{r}\frac{\partial p}{\partial \theta} + \frac{1}{Re_\lambda}\frac{\partial^2 u_\theta}{\partial x^2} +$$
$$\frac{1}{Re_\lambda}\frac{\partial}{\partial r}\left[\frac{1}{r}\frac{\partial(ru_\theta)}{\partial r}\right] + \frac{1}{r^2 Re_\lambda}\frac{\partial^2 u_\theta}{\partial \theta^2} + \frac{2}{r^2 Re_\lambda}\frac{\partial u_r}{\partial \theta}. \tag{S2.4}$$

The substitution of (2.6)-(2.7) into (S2.1)-(S2.4) leads to the base-flow equations (2.8)-(2.10) by collecting $\mathcal{O}(1)$ terms in the limits $k_x, Re_\lambda^{-1} \ll 1$ and $\mathcal{F} = \mathcal{O}(1)$. By collecting $\mathcal{O}(\varepsilon)$ terms, the boundary-region equations for the perturbation flow are found,

$$\frac{\partial \overline{u}_x}{\partial \overline{x}} + \frac{\overline{u}_r}{r} + \frac{\partial \overline{u}_r}{\partial r} + \frac{\overline{u}_\theta}{r} = 0, \tag{S2.5}$$

$$\left(-i + \frac{\partial U}{\partial \overline{x}} + \frac{m^2}{\mathcal{F}r^2}\right)\overline{u}_x + U\frac{\partial \overline{u}_x}{\partial \overline{x}} + \left(V - \frac{1}{\mathcal{F}r}\right)\frac{\partial \overline{u}_x}{\partial r} + \frac{\partial U}{\partial r}\overline{u}_r - \frac{1}{\mathcal{F}}\frac{\partial^2 \overline{u}_x}{\partial r^2} = 0, \tag{S2.6}$$

$$\left(-i + \frac{\partial V}{\partial r} + \frac{m^2 + 1}{\mathcal{F}r^2}\right)\overline{u}_r + U\frac{\partial \overline{u}_r}{\partial \overline{x}} + \left(V - \frac{1}{\mathcal{F}r}\right)\frac{\partial \overline{u}_r}{\partial r} + \frac{\partial V}{\partial \overline{x}}\overline{u}_x +$$
$$\frac{2}{\mathcal{F}r^2}\overline{u}_\theta + \frac{1}{\mathcal{F}}\frac{\partial \overline{p}}{\partial r} - \frac{1}{\mathcal{F}}\frac{\partial^2 \overline{u}_r}{\partial r^2} = 0, \tag{S2.7}$$

$$\left(-i + \frac{V}{r} + \frac{m^2 + 1}{\mathcal{F}r^2}\right)\overline{u}_\theta + U\frac{\partial \overline{u}_\theta}{\partial \overline{x}} + \left(V - \frac{1}{\mathcal{F}r}\right)\frac{\partial \overline{u}_\theta}{\partial r} + \frac{2m^2}{\mathcal{F}r^2}\overline{u}_r - \frac{m^2}{\mathcal{F}r}\overline{p} - \frac{1}{\mathcal{F}}\frac{\partial^2 \overline{u}_\theta}{\partial r^2} = 0. \tag{S2.8}$$

Equations (S2.5)-(S2.8) are also satisfied by $\left\{\overline{u}_x^{(0)}, \overline{u}_r^{(0)}, \overline{u}_\theta^{(0)}, \overline{p}^{(0)}\right\}$. The pressure and the spanwise velocity component are eliminated from (S2.7) and (S2.8) to find (2.11) and (2.12).

S3. Conditions at the pipe axis

In the cylindrical geometry, the pipe axis is a singularity in the equations of motion, but the velocity vector and the pressure must be regular there. Constraints on these

quantities must thus be satisfied, which leads to a specific behaviour of the Bessel-Fourier coefficients as the axis is approached and to the boundary conditions at the axis. We obtain the boundary conditions following the study of Lewis & Bellan (1990), discuss the regularity conditions found by Batchelor & Gill (1962) and Khorrami *et al.* (1989), and further analyze the problem according to Tuckerman (1989).

S3.1. *Boundary conditions at the pipe axis*

The boundary conditions for the perturbation flow at $r = 0$ are given in (2.28)-(2.30). The boundary conditions (2.28) for $m = 1$ involve the azimuthal velocity $\overline{u}_\theta$ and therefore (2.11)-(2.12) are solved together with the continuity equation (S2.5). For $m = 2$, there is no need to solve for the continuity equation; as $\overline{u}_r''$ is used as a new independent variable in the numerical solver, the last boundary conditions in (2.29) is replaced by $\overline{u}_r'' = 0$ because $\overline{u}_r$ grows linearly with r from the pipe axis at leading order (Lewis & Bellan 1990).

S3.2. *Symmetry and regularity at the pipe axis*

The radial behaviour of the velocity components found in Lewis & Bellan (1990) allows us to obtain the boundary conditions at $r = 0$ used to solve (2.11)-(2.12). Information on the velocity field can be inferred by imposing symmetry and regularity at the axis (Lewis & Bellan 1990). The streamwise velocity behaves as a scalar, i.e., $u_x \sim \hat{\psi}_m r^m e^{im\theta}$ as $r \to 0$. Lewis & Bellan (1990) explain that the radial and azimuthal velocity components do not behave as scalars at the axis and, by imposing regularity, they find $u_{r,m} \sim \hat{\lambda}_m r^{m-1} e^{im\theta}$, $u_{\theta,m} \sim i\hat{\lambda}_m r^{m-1} e^{im\theta}$ and $u_{r,m} + iu_{\theta,m} \to 0$ as $r \to 0$. When the vector is solenoidal, the last condition is verified exactly at $r = 0$. Our oncoming disturbance (2.1) and the solutions in region I, (3.19)-(3.21) and (3.31), all satisfy these conditions. For the gust disturbance, $\hat{\psi}_m = \hat{u}_{x,mn}^\infty (\xi_{mn}/4R)^m / \Gamma(m + 1)$ and $\hat{\lambda}_m = \hat{u}_{r,mn}^\infty (\xi_{mn}/2R)^{m-1} / [2^m \Gamma(m + 1)]$, while, in region I, we find $\hat{\lambda}_m = -2\hat{u}_{r,mn}^\infty J_m(\xi_{mn}/2) R^{1-m} e^{i\overline{x}} / \xi_{mn}$ for the leading-order components and $\hat{\lambda}_m = -\beta \hat{u}_{x,mn}^\infty J_m(\xi_{mn}/2) R^{1-m} / [2(2\overline{x}k_x R_\lambda)^{1/2}]$ for the next-order components.

Tuckerman (1989) further elucidates that, in order to guarantee regularity at the pipe axis, two conditions must be met when the velocity field Fourier-expands as $\hat{u} \sim r^{\hat{j}} e^{im\theta}$ when $r \to 0$, which is the behaviour that occurs for our free-stream disturbance (2.1) and in region I. For the streamwise component, i) $\hat{j} + m$ must be even and ii) $\hat{j} \geqslant m$, while, for the radial and azimuthal components, i) $\hat{j} + m$ must be odd and ii) $\hat{j} \geqslant \min\{m - 1, 2\}$. The number 2 in the last expression arises from imposing regularity on the Laplacian of the velocity vector. This condition is not strictly necessary for our inviscid free-stream and region-I disturbances, but we keep this restriction because these perturbations are utilized as initial conditions for the viscous boundary-region equations. In the last expression, Tuckerman (1989) also finds that $m+1$ must be considered together with $m - 1$ for the combination $u_{r,m} + iu_{\theta,m}$ (refer to her (5.4)), but in our specific case $u_{r,m} + iu_{\theta,m} \to 0$ because of continuity and therefore it is sufficient to consider $m - 1$. The boundary conditions are fully consistent with Tuckerman (1989)'s conditions. The asymptotic behaviours found by Lewis & Bellan (1990) all satisfy Tuckerman (1989)'s conditions and so do our oncoming disturbances and region-I solutions, as shown by using the exponent $\hat{j}$ of the Bessel-function expansions given by Abramowitz & Stegun (1972).

S3.3. *Independence of the velocity vector from the azimuthal angle at the pipe axis*

Batchelor & Gill (1962) and Khorrami *et al.* (1989) explain that the velocity field must be independent of the azimuthal angle as the pipe axis is approached, i.e., $\lim_{r \to 0} \partial \mathbf{u}/\partial \theta = 0$. This limit translates to the conditions i) $\partial u_x/\partial \theta = 0$, ii) $\partial u_r/\partial \theta - u_\theta = 0$, iii) $u_r + \partial u_\theta/\partial \theta = 0$. These conditions are satisfied by the free-stream gust (2.1), the solutions in region I found in §3.2.1, and our boundary conditions at the pipe axis.

For the free-stream gust, it is convenient to use the asymptotic expression $J_m(\bar{r}) \sim (\bar{r}/2)^m/\Gamma(m + 1)$ for $\bar{r} \ll 1$. Condition i) is satisfied when $m \neq 0$ because $J_m(0) = 0$ in these cases. Condition ii) is satisfied when $m = 0$ because $J_0'(0) = 0$, when $m = 1$ because the continuity condition (2.2) applies, and when $m > 1$ because both terms of the solutions are $\sim r^{m-1}$. Condition iii) is satisfied when $m = 0$ if we set $\hat{u}_{r,0n} = 0$, and when $m > 0$ for the same reasons as for condition ii). Condition (2.2) further agrees with the continuity check in equation (20) in Khorrami *et al.* (1989).

The leading-order solutions in region I, (3.22)-(3.24), satisfy the three conditions. Condition i) is satisfied because of (3.22a) and conditions ii) and iii) are satisfied for the same reasons as the gust velocity components because the potential (3.18) leads to velocity components that have the same asymptotic behaviour of the gust components as $r \to 0$. The solutions in region I arising from the potential (3.18) satisfy condition i), while conditions ii) and iii) are satisfied when $m = 0$ if $\hat{u}_{x,0n} = 0$, when $m = 1$ if $\hat{u}_{x,1n} = 0$, and always when $m > 1$ because the solution is $\sim r^{m-1}$.

The boundary conditions at the pipe axis can be found by imposing conditions i), ii), and iii) on (2.7). They apply to both $\overline{u}_x, \overline{u}_r, \overline{u}_\theta$ and $\overline{u}_x^{(0)}, \overline{u}_r^{(0)}, \overline{u}_\theta^{(0)}$. When $m > 0$ condition i) leads to $\overline{u}_x = 0$, condition ii) gives $m^2 \overline{u}_r + \overline{u}_\theta = 0$, and condition iii) gives $\overline{u}_r + \overline{u}_\theta = 0$. It follows that $\overline{u}_x = \overline{u}_r = \overline{u}_\theta = 0$ at $r = 0$ when $m > 1$. Similar to Khorrami *et al.* (1989), linearly dependent conditions occur when $m = 1$ and thus $\overline{u}_r + \overline{u}_\theta = 0$ in this case. These conditions are the same as those found following Lewis & Bellan (1990). L'Hôpital's rule is used on the continuity equation to find $2\partial \overline{u}_r/\partial r + \partial \overline{u}_\theta/\partial r = 0$ at $r = 0$ for every m (Khorrami *et al.* 1989). This condition is simplified to $\partial \overline{u}_r/\partial r = 0$ when $m \neq 2$ by use of the radial dependence found by Lewis & Bellan (1990).

S4. Negligible near-wall curvature effects

We demonstrate that the curvatures effects are negligible near the pipe entrance and near the wall (region II) when $Re_\lambda \gg 1$. This limit allows simplifying the Navier-Stokes equations in cylindrical coordinates (S2.1)-(S2.4) to the boundary-layer equations in Cartesian coordinates for both the base flow and the perturbation flow in the proximity of the wall. It follows that in region II the inner velocities $\{u_{x,in}, u_{r,in}, u_{\theta,in}\}$ are given by the Blasius solution for the base flow and by the solutions (4.13) on page 177 of Leib *et al.* (1999) for the boundary-layer perturbation flow.

The boundary-layer thickness is asymptotically smaller than the pipe radius, i.e., $\delta/R \ll 1$, which follows from $Re_\lambda \gg 1$. Since $y = R - r$, where y is measured from the pipe wall toward the pipe axis, we insert the following changes in (S2.1)-(S2.4): $r \to R$, $\partial/\partial r \to -\partial/\partial y$, $\partial^2/\partial r^2 \to \partial^2/\partial y^2$, $\theta \to z/R$, and $\{u_x, u_r, u_\theta\} \to \{u_{x,in}, -u_{r,in}, u_{z,in}\}$. The azimuthal modulation of the perturbation changes as $m\theta \to k_z z$, where $k_z = 2\pi$, because $m = 2\pi R = \mathcal{O}(1)$. The continuity equation (S2.1) immediately reduces to the Cartesian form. Besides the x-diffusion term that is negligible under the usual large-Re_λ assumption, the x-momentum equation (S2.2) has three viscous terms: i) $(RRe_\lambda)^{-1}\partial u_{x,in}/\partial y$, ii) $Re_\lambda^{-1}\partial^2 u_{x,in}/\partial y^2$, and iii) $Re_\lambda^{-1}\partial^2 u_{x,in}/\partial z^2$. Term ii) is asymptotically larger than the others because the near-wall scaling $y/\delta = \mathcal{O}(1)$

leads to $\delta \ll R$. The θ-momentum equation (S2.4) has one extra convective term and three viscous terms: i) $-u_{y,in}u_{z,in}/R$, ii) $Re_\lambda^{-1}\partial^2 u_{x,in}/\partial y^2$, iii) $Re_\lambda^{-1}\partial^2 u_{x,in}/\partial z^2$, and iv) $-2(RRe_\lambda)^{-1}\partial u_{y,in}/\partial z$. Like for the x-momentum equation, term ii) is asymptotically larger than the others because $\delta \ll R$. The y-momentum equation reduces to the vanishing wall-normal pressure gradient. The Cartesian boundary-layer equations are recovered, where the spanwise viscous effects are identically zero for the base flow and negligible for the perturbation flow.

S5. Inviscid base-flow Stokes streamfunction ψ_2

Equation (3.7) is solved by using the complex Fourier transform along x, whose inverse is

$$\psi_2(x,r) = \frac{1}{\sqrt{2\pi}} \int_{-\infty+i\gamma}^{+\infty+i\gamma} \hat{\psi}_2(\zeta,r)e^{i\zeta x}\mathrm{d}\zeta, \tag{S5.1}$$

where the use of $\gamma \in \mathbb{R} < 0$ is required to render $\sqrt{x}e^{\gamma x}$ absolutely integrable when $x > 0$. This integration path is necessary to define the complex Fourier transform of the boundary condition (3.8a). The function $\hat{\psi}_2$ satisfies $r\hat{\psi}_2'' - \hat{\psi}_2' - r\zeta^2\hat{\psi}_2 = 0$. The bounded solution that satisfies the boundary condition (3.8c) is $\hat{\psi}_2 = k_1(\zeta)rI_1(\zeta r)$ because the other solution proportional to the unbounded modified Bessel function of the second kind K_1 must vanish (the Frobenius method shows that it is not multiplied by r). By substituting the solution of $\hat{\psi}_2$ into (S5.1) and using the complex Fourier transform of (3.8a) and (3.8b), we find that

$$k_1(\zeta) = \frac{\beta\sqrt{2}}{I_1(\zeta R)} \int_0^\infty \sqrt{\xi}e^{-i\xi\zeta}\mathrm{d}\xi, \tag{S5.2}$$

where $\Im(\zeta) < 0$ for the integral in (S5.2) to be defined. The solution to (3.7) is

$$\psi_2(x,r) = \frac{\beta r}{\pi\sqrt{2}} \int_{-\infty+i\gamma}^{+\infty+i\gamma} \frac{I_1(\zeta r)e^{i\zeta x}}{I_1(\zeta R)} \int_0^\infty \sqrt{\xi}e^{-i\xi\zeta}\mathrm{d}\xi\mathrm{d}\zeta. \tag{S5.3}$$

The second integral, i.e., the complex Laplace transform which exists because $\gamma < 0$ (refer to page 401 of Dettman (1965)), leads to the final solution (3.11).

It is immediate to verify that (3.11) satisfies the boundary condition at the pipe axis, (3.8c). To verify that (3.8a) for $x > 0$ and (3.8b) for $x < 0$ are satisfied, the contour paths in the left and the right graphs of figure S1, are used, respectively. For both contour paths, the residue is zero because no poles are contained within the paths and the integral along the line l ($\Im(\zeta) = \gamma$) is (3.11) with $r = R$, i.e., the modified Bessel functions cancel out. In the left graph of figure S1, the integrals along l_1 and l_2 cancel out and the integrals along the arcs a_1 and a_2 tend to zero as the radius of the arcs R_a increases. Upon setting $\zeta = i\gamma + R_ae^{i\theta}$, $0 < \theta < \pi$, we note $|e^{i\zeta x}| = |e^{-\gamma x}e^{ixR_a(\cos\theta+i\sin\theta)}| = e^{-\gamma x}e^{-xR_a\sin\theta} \leqslant e^{-\gamma x}$, which justifies the choice of the arcs in that θ range and implies that

$$\int_{a_1,a_2} \frac{e^{i\zeta x}}{\zeta^{3/2}}\mathrm{d}\zeta \leqslant \frac{e^{-\gamma x}\pi R_a}{(R_a-\gamma)^{3/2}} \to 0 \quad \text{as} \quad R_a \to \infty. \tag{S5.4}$$

It follows that (3.11) with $r = R$ and $x > 0$ is equal to the opposite of the integral along the circle c in the left graph of figure S1. By changing the variable $\bar{\zeta} = i\zeta x$ in the integral along c, one finds the Hankel contour integral representation of the reciprocal of the gamma function, as shown on page 197 of Dettman (1965), which leads to (3.8a). When $x < 0$, (3.8b) follows immediately because the integral along the arc a_3 in the
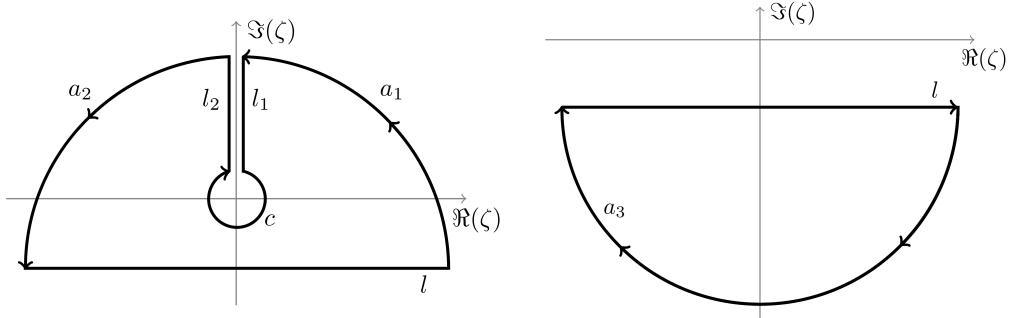
Figure S1: Contour paths of integration to verify that the solution (3.11) satisfies the boundary conditions (3.8*a*) ($x > 0$, left graph) and (3.8*b*) ($x < 0$, right graph).

right graph of figure S1 vanishes as R_a increases, following an argument analogous to the integrals along a_1 and a_2, the difference lying in the range $\pi < \theta < 2\pi$.

S6. Leading-order perturbation potential in region I

The solution to (3.15) that satisfies the boundary conditions (3.16) can be obtained by separation of variables when $x \gg 1$, i.e., $\phi = \hat{\phi}(r) \exp\left[ik_x(x - t) + im\theta\right]$, where the x dependence is found by matching with the gust (2.1). The quantity $\hat{\phi}(r)$ satisfies the modified Bessel equation (3.17) and is equal to

$$\hat{\phi}(r) = -\frac{\hat{u}_{r,mn}^{\infty} J_m(\xi_{mn}/2) I_m(k_x r)}{k_x R I_m'(k_x R)} = \mathcal{O}(1), \tag{S6.1}$$

where I_m is the modified Bessel function of order m. As $k_x \ll 1$, the asymptotic behaviour of the modified Bessel function for small argument, i.e., $I_m(k_x r) \sim \Gamma(m + 1)^{-1} \left(k_x r/2\right)^m$ (Abramowitz & Stegun 1972), is substituted into (S6.1) to find

$$\hat{\phi}(r) = -\frac{2R\hat{u}_{r,mn}^{\infty} J_m(\xi_{mn}/2)}{m\xi_{mn}} \left(\frac{r}{R}\right)^m, \tag{S6.2}$$

from which (3.18) is found. Solution (S6.2) is also found by solving the Euler differential equation that arises by neglecting the term proportional to $k_x^2 \ll 1$ in (3.15).

REFERENCES

ABRAMOWITZ, M. & STEGUN, I.A. 1972 *Handbook of Mathematical Functions*, Tenth edn. Dover, New York.
BATCHELOR, G.K. & GILL, A.E. 1962 Analysis of the stability of axisymmetric jets. *J. Fluid Mech.* **14** (4), 529–551.
CEBECI, T. 2002 *Convective Heat Transfer*. Springer-Verlag, Berlin Heidelberg.
DETTMAN, J.W. 1965 *Applied complex variables*. Courier Corporation.
HORNBECK, R.W. 1964 Laminar flow in the entrance region of a pipe. *Appl. Sci. Res.* **13**, 224–232.
KHORRAMI, M.R., MALIK, M.R. & ASH, R.L. 1989 Application of spectral collocation techniques to the stability of swirling flows. *J. Comp. Phys.* **81**, 206–229.
LEIB, S.J., WUNDROW, D.W. & GOLDSTEIN, M.E. 1999 Effect of free-stream turbulence and other vortical disturbances on a laminar boundary layer. *J. Fluid Mech.* **380**, 169–203.
LEWIS, H.R. & BELLAN, P.M. 1990 Physical constraints on the coefficients of Fourier expansion in cylindrical coordinates. *J. Math. Phys.* **31** (11), 2592–2596.

Tuckerman, L.S. 1989 Divergence-free velocity fields in nonperiodic geometries. *J. Comp. Phys.* **80** (2), 403–441.